

Spectral Energy Distributions of Dusty Galaxies

Toshinobu TAKAGI^{1,2,3} Vladas VANSEVIČIUS⁴ Nobuo ARIMOTO^{5,6}

¹ *Department of Physics, Rikkyo University, 3-34-1 Nishi-Ikebukuro, Toshima-ku, Tokyo 171-8501*

² *The Institute of Space and Astronautical Science, 3-1-1 Yoshinodai, Sagamihara, Kanagawa 229-8510*

³ *The Blackett Laboratory, Astrophysics Group, Imperial College, Prince Consort Road, London SW7 2BZ, UK*

t.takagi@ic.ac.uk

⁴ *Institute of Physics, Goštauto 12, Vilnius 2600, Lithuania*

⁵ *National Astronomical Observatory of Japan 2-21-1, Osawa, Mitaka, Tokyo 181-8588*

⁶ *Institute of Astronomy, School of Science, University of Tokyo 2-21-1, Osawa, Mitaka, Tokyo 181-0015*

(Received 0 0; accepted 0 0)

Abstract

We present a SED model of dusty galaxies, in which the equation of radiative transfer is solved by assuming spherical symmetry. The temperature fluctuation of very small dust particles is calculated consistently with the radiative transfer. The adopted dust model consists of graphite and silicate grains and PAHs, whose relative fractions are determined for each MW, LMC and SMC type extinction curve. This model allows us to derive the intrinsic SEDs of stellar populations embedded in dusty ISM, which are very important indicators for the age of stellar populations. Therefore, the evolutionary phase of starburst galaxies which have frequently very dusty ISM can be investigated with this SED model. We show that the SEDs of Arp220 and M82 can both be explained by the same single stellar population, despite the significant differences in the SEDs and the infrared luminosities. The apparent difference between their SEDs is mainly caused by the difference in the optical depth. In contrast, the SED of prototypical star-forming ERO, HR10, indicates that this galaxy is relatively old comparing to Arp220 and M82. It is found that, in the case of optically thin limit like elliptical galaxies, the optical depth cannot be inferred only from the SED, due to a degeneracy between the optical depth, galactic size, and the spatial distribution of dust; the latter two are important for estimating the average temperature of dust grains in elliptical galaxies. When the observed size of elliptical galaxies is adopted for the model geometry, SEDs can be used to constrain the spatial distribution of dust in elliptical galaxies.

Key words: dust, extinction — galaxies: ISM — galaxies: starburst — galaxies: stellar content – radiative transfer

1. Introduction

Age estimate of galaxies is one of the most important and essential tasks in modern astronomy, although difficult. Recent successive findings of high redshift galaxies allow age estimates of young galaxies to understand their formation processes. In this context, spectrophotometric evolutionary models of galaxies have been widely applied to derive ages of the high redshift galaxies such as 53W002 (Windhorst et al. 1991), B2 0902+34 (Lilly 1988; Bithell & Rees 1990; Windhorst et al. 1991; Eisenhardt & Dickinson 1992), 4C41.17 (Chambers & Charlot 1990; Chambers, Miley & van Breugel 1990; Windhorst et al. 1991; Graham et al. 1994; Lacy & Rawlings 1996; Dey et al. 1997), 6C1232+39 (Eales et al. 1993), B2 0920+34 (Chambers & Charlot 1990), and B2 1056+39 (Bithell & Rees 1990). However, the adopted photometric data for spectral energy distributions (SEDs) are mainly restricted to the UV-optical range in the rest frame, except for few galaxies. It turned out that in such cases the SED fitting is less helpful in order to determine uniquely the ages of these galaxies. This difficulty arises from the fact that the UV-optical SEDs of young stellar populations heavily obscured by dust are very similar to those of intrinsically old stellar populations; in other words, the UV-optical SEDs are degenerate in age and dust attenuation. In order to estimate the age of galaxies which contain a large amount of dust, it is necessary to analyse SEDs within a wide range of wavelengths including the dust emission (Takagi, Arimoto & Vasevičius 1999).

The importance of detailed modelling of dust effects on SEDs of galaxies has been demonstrated recently (e.g. Mazzei, De Zotti & Xu 1994; Gordon, Calzetti & Witt 1997; Vasevičius, Arimoto & Kodaira 1997; Silva et al. 1998; Efstathiou, Rowan-Robinson & Siebenmorgen 2000). However, the interpretation of the SEDs of dusty galaxies in the UV-NIR, which are the key to estimate the age of the stellar population (e.g. Takagi et al. 1999), is controversial. In the SED model by Silva et al. (1998), the SEDs of Arp220 and M82 in the UV-NIR are totally dominated by the relatively old stellar populations; i.e. unrelated to the very young stellar populations which are newly formed in recent starburst events. On the other hand, Efstathiou et al. (2000) show that the UV-NIR SED of M82 can be explained by the obscured young stellar populations. Although Silva et al. (1998) and Efstathiou et al. (2000) adopt the different photometric data with the different aperture size, this difference is not enough to explain the contradiction. Silva et al. (1998) divided the interstellar matter (ISM) of model galaxy into the star forming molecular clouds (MCs) and the diffuse medium. The formation process of stars is simulated, provided that stars are born only within the optically thick MCs and progressively escape from them. When the elapsing time from the onset of starburst is shorter than the time scale for stars to escape from MCs, all newly born stars are embedded in MCs and their light is completely hidden at the optical wavelengths, as they found for Arp220 and M82. Therefore, in their model, the contribution from starburst stellar populations to UV-NIR SEDs is negligible for any aperture size of these galaxies. Note that Efstathiou et al.

(2000) derive the age of starburst by applying the SED model, while Silva et al. (1998) assume the age of starbursts to reproduce observed SEDs.

The following observational results provide important clues to the origin of the UV-NIR light of starbursts: 1) Rakos, Maindl & Schombert (1996) showed that the UV-optical SEDs of starburst galaxies are dominated by strongly reddened, young stellar populations; 2) Schmitt et al. (1997) demonstrated that UV-NIR SEDs of starburst galaxies are different from those of normal galaxies; 3) Meurer et al. (1997) showed a tight correlation between the UV spectral slope and the ratio of FIR flux to UV flux; 4) Goldader et al. (1995) showed that the $2 \mu\text{m}$ continua of the ten ultraluminous infrared galaxies are dominated by red supergiants in starburst stellar populations, by using the CO indices of these galaxies. All these observations indicate a significant contribution of the starburst population to the UV-NIR SEDs of starburst galaxies. Therefore, in this paper, the UV-NIR SEDs consistently coupled with FIR-submm SEDs are used to estimate the age of starburst galaxies. In this way, it should be possible to reduce the uncertainties of estimated age considerably.

The SED of starburst galaxies has sometimes been modelled by using the empirical relation between IRAS colours and total IR luminosities (e.g. Devriendt, Guiderdoni & Sadat 1999; Totani & Takeuchi 2002). We would like to point out a vital importance of solving the radiative transfer problem in SED modelling, since it is the only method to employ the relations between the SED features in the whole wavelength range and physical parameters of the galaxies and dust consistently. Therefore, some additional spectral information is very helpful in order to constrain physical parameter space allowed for fitting, e.g. the silicate absorption feature at $9.7 \mu\text{m}$ arising due to the self-absorption by dust, can be used to constrain the type of extinction curve in our model.

Here, we present a SED model of dusty galaxies by solving the equation of radiative transfer, in which stars are diffusely distributed within a spherical region. This assumption for geometry is clearly different from those by Efstathiou et al. (2000) in which a starburst region is modelled as an ensemble of star-forming molecular clouds. The Hubble Space Telescope (HST) revealed that most of nearby starburst galaxies actually have clusters of newly formed massive stars (O’Connell, Gallagher & Hunter 1994; Meurer et al. 1995; Tacconi-Garman, Sternberg & Eckart 1996), so-called super star clusters (SSCs). However, Meurer et al. (1995) reported that the SSCs contribute only 20% of the UV luminosity on average. Thus, UV light from starburst region is dominated by the light from diffusely distributed stars as modelled here, rather than that from star clusters. Also, note that Shioya, Taniguchi & Trentham (2001) suggest that in Arp220 the contribution from SSCs to the bolometric luminosity is at most 20%.

Even if the observed SED of a galaxy is reproduced by the SED models, it is important to verify the uniqueness of the solution. Generally, a sophisticated handling of the SED model of dusty galaxies requires a number of parameters. In such a case, all the parameters may not be determined from the SED fitting alone; thus, the solution may not be unique. Therefore, it

is important to investigate the dependence of SEDs on each parameter. Once these test results are obtained, it becomes clear which parameters can be determined from the SED fitting.

In this paper, we first intend to study the basic properties of SEDs of dusty galaxies, which are helpful to have an insight on what physical parameters can be constrained with the specific properties of SEDs. Then, we apply our SED model to dusty galaxies, a representative of the most active starburst (Arp220), a nearby less luminous starburst (M82), a distant extremely red star-forming galaxy (HR10), and an elliptical galaxy (NGC2768) as a study for optically thin case. Specifically, we focus on the starburst age of dusty starbursts derived from UV-submm SEDs.

This paper is organized as follows. The model description and the SED analysis of parameter sensitivity are given in §2 and §3, respectively. Then, we apply our model to the observed SEDs in §4. Discussion and conclusions are given in §5 and §6, respectively. The cosmological parameters adopted throughout this paper are $H_0 = 75 \text{ km s}^{-1} \text{ Mpc}^{-1}$, $\Omega = 1$ and $\Lambda = 0$.

2. Model

We have developed a code which solves the equation of radiative transfer by assuming spherical symmetry for arbitrary radial distributions of stars and dust. Isotropic multiple scattering is assumed and the self-absorption of re-emitted energy from dust is fully taken into account. The adopted dust model takes into account graphite and silicate grains, and polycyclic aromatic hydrocarbons (PAHs). We successfully reproduce the typical extinction curves in Milky Way (MW), Large and Small Magellanic Cloud (LMC and SMC) as well as the spectra of cirrus emission in the MW, which are modelled by considering the temperature fluctuation of very small grains and PAHs. As an input to our modelling, the intrinsic stellar SEDs of galaxies are taken from Kodama & Arimoto (1997). We assume that the SEDs of galaxies are dominated by the starburst region or by the diffusely distributed stars and dust: the former case is for starburst galaxies and the latter one for elliptical galaxies. In both cases the adopted geometry is defined by the radial distribution of stars and dust with different scale lengths.

2.1. *Stellar Spectral Energy Distribution of Galaxies*

An evolutionary synthesis code developed by Kodama & Arimoto (1997), which gives consistent chemical and spectral evolution of a galaxy, is used for generating the intrinsic stellar SEDs. The basic structure of the code follows Arimoto & Yoshii (1986) prescription, i.e. the effects of stellar metallicity are explicitly taken into account in calculating galaxy spectra. The characteristics of this model are as follows.

- New stellar evolutionary tracks are incorporated comprehensively (VandenBerg et al. 1983; Bressan, Chiosi, & Fagotto 1994; Fagotto et al. 1994a, 1994b) and late stellar evolutionary

stages (horizontal branch - Yi 1996; asymptotic giant branch [AGB] - Vassiliadis & Wood 1993; post-AGB and white dwarf - Vassiliadis & Wood 1994) are fully included

- For the stellar spectra, Kurucz’s (1992) stellar flux library is used for the metallicity $0.0001 \leq Z \leq 0.05$, the effective temperature $4000 \text{ K} \leq T_{\text{eff}} \leq 50000 \text{ K}$, and the surface gravity $0.0 \leq \log g \leq 5.0$. The library covers the wavelength range from 9 nm to $3.2 \mu\text{m}$ with the spectral resolution $\Delta\lambda = 1 \text{ nm} - 2 \text{ nm}$ for $\lambda \leq 1 \mu\text{m}$ and $\Delta\lambda = 5 \text{ nm} - 10 \text{ nm}$ for $\lambda > 1 \mu\text{m}$.
- The spectra of cool stars with $T_{\text{eff}} \leq 4000 \text{ K}$ are taken from Pickles (1985) and Gunn & Stryker (1983).

Throughout this paper, we adopt the model of simple stellar populations (SSPs) with solar metallicity as the intrinsic stellar SED model, otherwise noted explicitly. We adopt the Salpeter initial mass function (IMF) with stellar masses ranging from $0.1 M_{\odot}$ to $60 M_{\odot}$. Some examples of SEDs of SSPs are shown in Figure 1. In general, the intrinsic SEDs of stellar populations are mainly determined by both the age and the star formation history. Therefore, in order to derive the definite age of stellar populations from the SED, it is necessary to determine the time scale of star formation, which can be expressed in terms of the dynamical time, sound-crossing time, and cooling time. In this study, we mainly focus on starburst galaxies, in which the variation of stellar populations is less significant, comparing to normal spiral galaxies. Even in such an extreme case, it is difficult to know the characteristic time scale of each starburst event. Therefore, we choose the simplest stellar population as an indicator of the age of starbursts, rather than try to determine precise ages of starbursts from intrinsic stellar SEDs.

Gas emission is not taken into account in our model which is designed to calculate the continuum emission of galaxies. A modification of SEDs due to the gas emission is not significant, unless a galaxy is younger than 10 Myr for SSPs (Leitherer & Heckman 1995; Fioc & Rocca-Volmerange 1997). As we will show later, our model can reproduce the observed SEDs of dusty galaxies with the age of SSP older than 10 Myr. Therefore, we believe that the effect of gas emission does not affect our conclusions.

2.2. Dust model

2.2.1. Optical Properties

The optical properties of graphite and silicate are taken from Laor & Draine (1993). We adopt a "smoothed astronomical silicate" which is obtained by removing the absorption feature at $1/\lambda = 6.5 \mu\text{m}^{-1}$ from the imaginary part of the original dielectric function (Draine & Lee 1984; Laor & Draine 1993; Weingartner & Draine 2001).

Optical properties of PAH are adopted according to Léger, d’Hendecourt & Défourneau (1989), and Désert, Boulanger & Puget (1990). The PAH features are assumed to have the Lorentz profile, which successfully reproduced the spectra of the reflection nebula NGC7023

and the Ophiuchus molecular cloud observed by ISO (Boulanger et al. 1998). The Lorentz function is given by:

$$F(\nu) = Af(\nu) = \frac{A}{\pi\Gamma} \left[1 + \left(\frac{\nu - \nu_0}{\Gamma} \right)^2 \right]^{-1}, \quad (1)$$

where $f(\nu)$ is the normalized Lorentz profile, and A is the integrated cross-section, and ν_0 and Γ give the frequency and the width of the band, respectively. The adopted parameters for the PAH features at $\lambda = 3.3, 6.2, 7.7, 8.6, 11.3$ and $12.7 \mu\text{m}$ are given in Table 1. The number of H atoms attached to a PAH molecule is given by $N_H = x_H(6N_C)^{1/2}$, where x_H (≤ 1 by definition) is the degree of dehydrogenation, and N_C is the number of carbon atoms in one PAH molecule (Omont 1986). Since the binding energy of C-H bond is weaker than that of C-C bond, the H atoms tend to be removed in the strong radiation field. This suggests that x_H could vary with the strength of radiation field. However, recent observations showed that relative intensities of PAH features are independent of the strength of radiation field (Lemke et al. 1998; Chan et al. 2001). Thus, it is too early to introduce the relation between x_H and the strength of radiation field, instead we assume $x_H = 0.4$ according to Désert et al. (1990).

2.2.2. Size Distribution

The spectra of diffuse high latitude clouds (so-called Galactic cirrus), obtained by the IRAS all-sky survey (Low et al. 1984), show excesses of emission at 12 and 25 μm over those expected from dust grains radiating at the equilibrium temperature. Draine & Anderson (1985) suggested that the excessive emission at MIR could be radiated by grains small enough to undergo the temperature fluctuation in the local interstellar radiation field, due to their small heat capacity. Such very small grains (VSGs), typically smaller than 0.01 μm , are transiently heated up to several hundreds of Kelvin by the interstellar radiation field and emit in the MIR. Hereafter, we define both graphite and silicate grains with the radii $a < 0.01 \mu\text{m}$ and $a > 0.01 \mu\text{m}$ as VSGs and big grains (BGs), respectively.

For BGs, we adopt a power law size distribution derived by Mathis, Rumpl & Nordsieck (1977, hereafter MRN). For VSGs, the same size distribution is adopted, but with the different index (Draine & Anderson 1985). Introducing the radius $a_b = 0.01 \mu\text{m}$, at which a break between the two power laws takes place, the size distribution is given by:

$$dn_k = \begin{cases} n_H C_k a_b^\beta (a/a_b)^{\gamma_k} da, & \text{for } a_{min} < a < a_b \text{ (VSGs)} \\ n_H C_k a^\beta da, & \text{for } a_b < a < a_{max} \text{ (BGs)} \end{cases} \quad (2)$$

where dn_k is the number density of grains of type k ($k = g$ for graphite and $k = s$ for silicate) in the interval $[a, a + da]$, n_H is the number density of H nuclei, and C_k is the coefficient which determines the ratio of dust to hydrogen. For both graphite and silicate grains, we adopt $\beta = -3.5$, $a_{min} = 0.001 \mu\text{m}$, $a_b = 0.010 \mu\text{m}$ and $a_{max} = 0.25 \mu\text{m}$. The indices of VSG size distribution γ_k are determined by the fits to the MW extinction curve and the spectrum of Galactic cirrus.

For PAHs, we write the size distribution as a power law of N_C :

$$dn_P = n_H C_P N_C^{\gamma_P} dN_C, \quad \text{for } N_{C1} < N_C < N_{C2}, \quad (3)$$

where N_{C1} and N_{C2} are the number of C atoms in the smallest and largest PAH, respectively. We use the subscription $k = P$ for PAHs. Since the small PAHs with $N_C < 20$ will evaporate even in the weak radiation field like the local interstellar radiation field (Omont 1986), $N_{C1} = 20$ is adopted in this work. On the other hand, N_{C2} is less constrained. N_{C2} should be less than ~ 1000 so that a single photon could heat up PAHs to the temperature at which the emission peak is located at MIR (Puget & Léger 1989). We assume that the smallest graphite grain and the largest PAH contain the same number of C atoms (see also Dwek et al. 1997). According to the relation between a and N_C :

$$a(\mu\text{m}) = \begin{cases} 1.29 \times 10^{-4} N_C^{1/3}, & \text{for graphite grains} \\ 10.0 \times 10^{-4} (N_C/120)^{1/2}, & \text{for PAHs} \end{cases} \quad (4)$$

we get $N_{C2} = 465$ for $a_{min} = 0.001 \mu\text{m}$. It is assumed that γ_P is equal to the index of size distribution of graphite VSGs, which is written as a function of N_C . Using above relations between a and N_C , γ_P is given by $(\gamma_g - 2)/3$.

2.2.3. Temperature Fluctuation

When the dust grains attain temperature equilibrium with a surrounding radiation field, J_λ , by radiating the same amount of energy as the absorbed one, the equilibrium temperature, T_{eq} , is determined by:

$$4\pi \int \sigma_{\lambda,k}^a(a) J_\lambda d\lambda = 4\pi \int \sigma_{\lambda,k}^a(a) B_\lambda(T_{eq}) d\lambda, \quad (5)$$

where $\sigma_{\lambda,k}^a(a)$ is the absorption cross-section of dust grains of type k and size a , and B_λ is the Planck function.

When dust particles are small enough, grains cannot attain the temperature equilibrium with the interstellar radiation field. In this case, we have to calculate the temperature distribution function dP/dT , which is the probability for finding a particle in the interval $[T, T + dT]$, in order to predict the emission spectra. Methods to calculate dP/dT have been presented by several authors (Draine & Anderson 1985; Désert, Boulanger & Shore 1986; Dwek 1986; Guhathakurta & Draine 1989). We follow the method outlined by Guhathakurta & Draine (1989), in which the transition matrix is defined as the probability per unit time of a particle making a transition in the enthalpy space by the emission or absorption, and the solution is derived by inverting this transition matrix. The heat capacities of graphite and silicate are also taken from Guhathakurta & Draine (1989). For PAHs, the same heat capacity is used as that of graphite. Although the different expressions are given for its heat capacity (e.g. Léger et al. 1989; Dwek et al. 1997), alternative choice has no significant influence on the emission spectra (Siebenmorgen & Krügel 1992). By using dP/dT , the emissivity per dust particle with the size a and the constituent k is given by:

$$\varepsilon_{\lambda,k}(a) = 4\pi\sigma_{\lambda,k}^a(a) \int_0^{T_{sub,k}} B_{\lambda}(T) \frac{dP_k}{dT}(a, T) dT, \quad (6)$$

where the sublimation temperature $T_{sub,k} = 800$ K is assumed for all the dust constituents according to Carico et al. (1988) who showed that the emission from hot-dust particles with the temperature of ~ 800 K contributes to the NIR luminosity of IRAS bright galaxies. This assumption is safe because, unless $T_{sub,k}$ is higher than 800 K and the starburst is younger than 10 Myr, the resulting SEDs depend little on $T_{sub,k}$. If we adopt $T_{sub,k}=1500$ K (c.f. Kobayashi et al. 1993), a little excess of emission ($< 10\%$) can be seen in the NIR wavelengths only for the optically thick cases in which dust emission dominates the NIR emission, and therefore this effect is negligible to the results of SED fitting. In case of the temperature equilibrium, dP/dT is given by the delta function $\delta(T - T_{eq})$.

2.2.4. Dust in the MW, LMC and SMC

Figures 2 and 3 show the model fits to the extinction curve and the spectrum of cirrus emission in the MW, respectively. The extinction curve is given by the cross-section per hydrogen atom:

$$\sigma_{\lambda}^H = \frac{1}{n_H} \sum_k \int \sigma_{\lambda,k}^e(a) \frac{dn_k}{da} da, \quad (7)$$

where $\sigma_{\lambda,k}^e(a)$ is the extinction-cross section of the type k and size a dust grains. The adopted interstellar radiation field is taken from Mathis, Mezger & Panagia (1983). The contribution of PAHs to the spectrum and the extinction curve is significant; they dominate the spectrum at $\lambda < 12 \mu\text{m}$, and are responsible for the nonlinear extinction rise at FUV. The predicted extinction at FUV is a factor of two higher than the average extinction curve in the MW. The dust model presented by Dwek et al. (1997), in which the same optical properties are adopted, also overestimates the FUV extinction curve. Unfortunately, as far as the visible-UV absorption of PAHs in the gas phase is concerned, very few studies are available especially for the large PAHs (Verstraete & Léger 1992). We think, this discrepancy should be solved by using the more reliable optical properties of PAHs than those available at present.

Since the cirrus spectra of the LMC and SMC are not available at present, only the extinction curves are used to derive relative grain fractions, provided that fraction ratios of carbonaceous particles (graphite BGs, VSGs and PAHs) are the same as those of the MW (see also Pei 1992). The model fits to the extinction curve in the LMC and SMC are also shown in Figure 2. For normalisation of the extinction curves, the adopted ratios of hydrogen column density to colour excess $E(B - V)$ are $5.8 \cdot 10^{21}$, $2.0 \cdot 10^{22}$, and $4.6 \cdot 10^{22}$ for the MW, LMC, and SMC, respectively (Mathis 1990). In Table 2, we give the derived mass ratios of dust to hydrogen and the relative mass fractions of various constituents of dust. Note that the fraction of VSGs of type k , f_k^{VSG} and that of BGs, f_k^{BG} , are related by:

$$\frac{f_k^{VSG}}{f_k^{BG}} = \frac{\beta + 4}{\gamma_k + 4} \frac{a_b^{\gamma_k+4} - a_{min}^{\gamma_k+4}}{a_{max}^{\beta+4} - a_b^{\beta+4}}. \quad (8)$$

It is difficult to determine the amount of silicate VSGs, because they have little influence on both of the extinction curve and the spectrum of cirrus emission. Therefore, we simply extend downward the lower end of MRN distribution from a_b to a_{min} for silicate, i.e. $\gamma_s = \beta$. For graphite VSGs, we derive $\gamma_g = -3.75$.

2.3. Radiative Transfer

2.3.1. Geometry

The density distributions, $\rho(r)$, of stars and dust are assumed to be given by King's law:

$$\rho(r) = \frac{\rho_0}{\left(1 + \left(\frac{r}{r_c}\right)^2\right)^{\frac{3}{2}}}, \quad (9)$$

where ρ_0 is the density at the centre of galaxy and r_c is a core radius. We fix a geometry of stars and change the dust distribution by choosing a value of parameter $\eta \equiv r_{c,D}/r_{c,S}$, where $r_{c,S}$ and $r_{c,D}$ are the core radius of stars and dust, respectively.

The second parameter that defines the geometry is a tidal radius r_t which determines ρ_0 with a given total mass. When the total mass of stars is fixed, the temperature of dust is controlled by the tidal radius of stars $r_{t,S}$, since the energy density of the radiation field is approximately proportional to the stellar density. In order to keep a source function (see below) constant, we adopt a mass-radius relation:

$$r_{t,S} = 10R \left(\frac{M_*}{10^{11}M_\odot} \right)^{0.5} \quad [\text{kpc}], \quad (10)$$

where M_* is the total stellar mass and R is a scaling factor, and the normalisation is given for the scale of typical galaxy. Note that, for constant value of R , the relative shape of SED is conserved for different M_* due to this relation, when the optical depth is kept constant. We assume that the tidal radius of dust $r_{t,D}$ is the same as $r_{t,S}$, i.e. $r_{t,D}=r_{t,S}(=r_t \text{ hereafter})$, and there is no dust at $r > r_t$. We adopt the concentration parameter $c \equiv \log(r_t/r_{c,S}) = 2.2$, which is the typical value for normal elliptical galaxies (Combes et al. 1995). This value is also adopted for starburst galaxies in which the real distribution of stars inside the dominant starburst regions is difficult to derive due to the effect of dust attenuation. However, the effects of c on the SED are marginal, and detectable only at MIR region, and therefore have negligible impact on the values of parameters derived in §4.

The dust distributions $\rho_D(r)$ for $\eta = 1, 10, 100$, and 1000 are shown in Figure 4. Note that, for larger values of η , r_t can be smaller than $r_{c,D}$, due to the definition given above. In the case of $\eta = 1000$, dust distributes nearly uniformly and surrounds centrally concentrated stars, while in the case of $\eta = 1$, stars and dust are distributed identically. The former case is similar to the shell geometry suggested for starburst galaxies by Gordon, Calzetti & Witt (1997). However, note that the shell geometry gives SEDs different from our case if $\eta = 1000$ and $\tau_V \gg 1$, since the shell geometry results in the spectral cut-off around NIR (see the results by Rowan-Robinson & Efstathiou 1993).

A mass of dust, M_D , can be derived as follows. The optical depth at V band is defined by:

$$\tau_V = \int_0^{r_t} n_H(r) \sigma_V^H dr, \quad (11)$$

where $n_H(r)$ is the number density of hydrogen and σ_V^H is the extinction cross-section of dust per hydrogen at V band. A total number (or total mass) of hydrogen is derived by using the distribution function defined by η , once τ_V is specified. The mass ratio of dust to hydrogen is determined by the dust model. Since the column density is proportional to r_t^{-2} for a given mass, M_D is given by:

$$M_D = M_0 \frac{\tau_V}{\tau_0} \left(\frac{r_t}{10 \text{ kpc}} \right)^2, \quad (12)$$

where both M_0 and τ_0 are the normalisation factor. By using the dust model described in §2.2 for the MW, LMC and SMC, M_0 is found to be $5.5 \cdot 10^7 M_\odot$, $9.4 \cdot 10^7 M_\odot$ and $1.1 \cdot 10^8 M_\odot$, respectively. The second normalisation factor τ_0 depends on the geometry and is equal to 1.0, 1.78, 33.86, and 1753 for $\eta = 1000, 100, 10,$ and 1 , respectively.

2.3.2. Method of Calculation

Solving the equation of radiative transfer for an arbitrary radial distribution of stars and dust, we adopt the "method of rays" (Band & Grindlay 1985). The schematic picture of this method is shown in Figure 5.

It is convenient to divide the specific intensity, I_λ , into three components,

$$I_\lambda = I_\lambda^{(1)} + I_\lambda^{(2)} + I_\lambda^{(3)}, \quad (13)$$

where the superscripts (1), (2) and (3) represent direct light from stars, scattered light by dust grains, and thermal emission from dust grains, respectively (Rowan-Robinson 1980). In the case that the optical properties of dust grains are independent of their temperature, each component of intensity can be calculated independently in the order of the superscript. The details of iterative calculation of $I_\lambda^{(2)}$ and $I_\lambda^{(3)}$ are discussed in the following subsections.

The differential equation for the specific intensity, I_λ , along a ray is given by:

$$\frac{dI_\lambda(b, s)}{ds} = -n_H(r) \sigma_\lambda^H [I_\lambda(b, s) - S_\lambda(r)]. \quad (14)$$

The impact parameter to the centre, b , and path length along the ray, s , are related to the radial distance, r , according to an expression:

$$r^2 = b^2 + (\sqrt{r_t^2 - b^2} - s)^2. \quad (15)$$

The source function for $I_\lambda^{(1)}$ is given by:

$$S_\lambda^{(1)}(r) = \frac{\varepsilon_\lambda^*(r)}{4\pi n_H(r) \sigma_\lambda^H}, \quad (16)$$

where $\varepsilon_\lambda^*(r)$ is the emissivity of stellar component at wavelength λ .

Spherical geometry of the model requires only radial grid to be specified. The grid is defined by:

$$r_j = \left(\frac{j-1}{N-1} \right)^d r_t, \quad (17)$$

where N is the total number of radial shells and d is a parameter that depends on the dust distribution. The required N depends on the adopted τ_V . In all analysed cases, the grid with $d = 3$ and $N = 160$ gave results with satisfying accuracy; i.e. the difference between the input and output energy is less than 5% (see §2.3.4). If the required accuracy is violated the finer grid should be redefined.

For each $b_j (= r_j)$, $I_\lambda^{(1)}$ is calculated at the crossing points of the ray and shells' boundaries. The grid of path length, s_i , is defined at these points. Then, the equation for j -th ray is written as:

$$I_\lambda^{(1)}(b_j, s_{i+1}) = \bar{S}_i + e^{-\Delta\tau_i} (I_\lambda^{(1)}(b_j, s_i) - \bar{S}_i), \quad (18)$$

with the boundary condition $I_\lambda^{(1)}(b_j, s_1) = 0$, where $\Delta\tau_i = (s_{i+1} - s_i) \bar{n}_H \sigma_\lambda^H$, and the bar above variables indicates an average of i -th and $(i+1)$ -th values. Once $I_\lambda(b_j, s_i)$ is calculated for all j ($1 < j < N$) and i ($1 < i < 2(N-j) + 1$), one can derive the mean intensity in case of spherical geometry:

$$J_\lambda^{(1)}(r) = \frac{1}{2} \int_{-1}^{+1} I_\lambda^{(1)}(r, \mu) d\mu, \quad (19)$$

or

$$J_\lambda^{(1)}(r_{j'}) = \frac{1}{2} \sum_{j=1}^{j'-1} (\bar{I}_\lambda^{(1)}(b_j, s_{j+}) + \bar{I}_\lambda^{(1)}(b_j, s_{j-})) \Delta\mu_j, \quad (20)$$

where $\Delta\mu_j$ is the step of cosine grid, μ_j , which is defined by the angle between the vector pointing the direction of the j -th ray through the radial point $r_{j'}$ (\mathbf{v} in Figure 5) and the radius vector; s_{j+} and s_{j-} are the path lengths of the ray defined by b_j , from both sides of the outer edge to the shell $r_{j'}$, which means $j+ = N + (j' - 1) - 2(j - 1)$ and $j- = N - (j' - 1)$; the bar above I_λ means average of the j -th and $(j+1)$ -th values.

The components, $I_\lambda^{(2)}$ and $I_\lambda^{(3)}$, are calculated in a similar manner by using the source function characteristic for each component.

2.3.3. Scattered Light

The source function of n -times scattered light is:

$$S_{\lambda,n}^{(2)}(r, \mathbf{n}) = \frac{\omega_\lambda}{4\pi} \int g(\mathbf{m}, \mathbf{n}) I_{\lambda,n-1}^{(2)}(r, \mathbf{m}) d\Omega, \quad (21)$$

where $I_{\lambda,n-1}^{(2)}$ is the intensity of $(n-1)$ -times scattered light, $g(\mathbf{m}, \mathbf{n})$ is the angular phase function for coherent scattering from direction \mathbf{m} to \mathbf{n} , and ω_λ is a dust albedo (e.g. Mihalas 1978). Isotropic scattering is assumed for simplicity, that means $g(\mathbf{m}, \mathbf{n}) \equiv 1$. The total

intensity of scattered light, $I_\lambda^{(2)}$ is given by $\sum_n I_{\lambda,n}^{(2)}$. Since $I_\lambda^{(1)}$ can be regarded as the 0-times scattered light, the source function of once scattered light in the case of spherical geometry is:

$$S_{\lambda,1}^{(2)}(r) = \frac{\omega_\lambda}{4\pi} \int I_{\lambda,0}^{(2)}(r, \mathbf{n}) d\Omega = \frac{\omega_\lambda}{2} \int_{-1}^{+1} I_\lambda^{(1)}(r, \mu) d\mu. \quad (22)$$

Using this definition of the source functions, the intensities of the higher terms of scattered light are calculated by using the method given in the previous section. When the number of scattering terms considered is not sufficient, this results in a loss of the output energy. We find that the losses are less than 0.3% for the MW extinction curve when up to six terms are taken into account.

In Figures 6 and 7, the mean intensity ratios of n to $n - 1$ times scattered light as a function of r are shown for different η and τ_V in the case of $\omega = 0.6$. Generally, the mean intensity ratio approaches to a flat distribution for the higher order of scattered light. For large τ_V , this mean intensity ratio is hard to become totally constant from $r = 0$ to r_t , due to the slow diffusion of photons. Figure 8 shows the fraction of the unabsorbed stellar light (direct light) and the emerging scattered light both normalized with respect to the total input luminosity for the uniform distribution of stars and dust (Table 3A in Witt, Thronson & Capuano 1992). In our calculation, both values of the direct and scattered light are systematically smaller in comparison with the results obtained by Witt et al. (1992) who solved the radiative transfer problem by using the Monte Carlo method. The analytic solution for the direct light in an optically thick case is given by Band & Grindlay (1985) and is plotted together. Our results are consistent with the analytic solution. In Figure 9, luminosity ratios of scattered to direct light are compared. The results of Witt et al. (1992) are plotted by circles, while ours are represented by solid lines. Each solid line corresponds to a particular number of scattering terms used for calculation of the scattered light. Over the whole range of τ_V , the results of Witt et al. (1992) are consistent with ours when the first five scattering terms are taken into account.

2.3.4. Self-absorption

In order to take into account a self-absorption of dust emission, the radial distribution of dP/dT , is iteratively calculated for every constituent and every discrete grain size until the energy conservation is fulfilled. The first guess of dP/dT , which is denoted as dP/dT_1 , is done using the mean intensity calculated from only two components, $I_\lambda^{(1)}$ and $I_\lambda^{(2)}$. With the assumption that the scattering of dust emission is negligible, the source function for the n -th guess of the thermal component of intensity, $I_{\lambda,n}^{(3)}$, is given by:

$$S_{\lambda,n}^{(3)}(r) = \frac{1}{n_H(r)\sigma_\lambda^H} \sum_k \int \int_0^{T_{sub,k}} \sigma_{\lambda,k}^a(a) B_\lambda(T) \frac{dP_k}{dT}(a, T, r) dT \frac{dn_k}{da} da. \quad (23)$$

Calculation of the $I_{\lambda,n}^{(3)}$ is performed in the same way as described in §2.3.2. The sum of intensities, $I_\lambda^{(1)} + I_\lambda^{(2)} + I_{\lambda,n}^{(3)}$ is used to derive dP/dT_{n+1} . The mean temperature of dust rises step

by step during the iterative procedure. We continue the iteration until the energy conservation is fulfilled. Even in the worst cases ($\tau_V \sim 40$), the grid can be adjusted to keep the "numerical" losses of the total energy below 5%. This numerical loss is less than 3% in the nominal case.

The changes of the spatial distribution of equilibrium temperature of BGs, $T_{eq}(r)$, and the SED due to the self-absorption are shown in Figure 10, panels a and b, respectively. Heating dust by the thermal emission of dust itself, i.e. the self-absorption, has considerable effect on the MIR emission if τ_V is larger than ~ 10 . The effect of self-absorption is most prominent in a case of the SMC extinction curve since it has the largest absorption cross section at MIR due to high fraction of silicate grains.

Ivezić et al. (1997) have defined a set of benchmark problems and gave exact solutions suitable for verification of the radiative transfer codes dealing with dusty environments. The benchmark problems are solved with a central point source embedded in a spherically symmetric dust envelope with an inner cavity being free of dust. The density variation with r is assumed to be a power law, $\rho(r) \propto r^{-p}$. We show the results of comparison with $p = 0$ in Figure 11. The consistency is very good although, in the extreme case of $\tau_{1\mu\text{m}} = 1000$, the temperature of dust is slightly higher than the benchmark solution. By the definition of the benchmark problem, the radius of inner cavity, r_1 , has to be adjusted during the iteration to keep the dust temperature at the inner edge of dust envelope equal to 800 K. However, we do not adjust the inner radius since we do not need such rigorous adjustment for the purpose of galaxy modelling. As a result, our temperature is slightly higher (~ 830 K) due to the heating by the scattered light and dust emission. This mutual heating of dust is negligible when $\tau_{1\mu\text{m}} \leq 100$. On the other hand, in the case of $p = 2$, the effect of mutual heating is larger due to more pronounced concentration of the dust near the inner radius of the shell than the case of $p = 0$. In this case, the adjustment of the inner radius of dusty zone is indispensable to compare the results properly with the benchmark solutions.

3. Sensitivity Analysis

It is necessary to know how the resulting SEDs depend on the model parameters such as age t , optical depth τ_V , core radius ratio η , size scaling factor R , and type of the extinction curve, in order to judge whether the results of SED fitting are unique or not. In this section, we describe how the radial temperature distributions and the SEDs depend on these parameters. The standard model is defined by a set of parameters $t = 10$ Myr, $\tau_V = 1.0$, $\eta = 1000$, $R = 1.0$, and the MW type extinction curve, as tabulated in Table 3. Unless otherwise stated, the standard model parameters are used throughout this section.

3.1. The Effect of Age

Figure 12a shows the radial temperature distribution $T_{eq}(r)$ of models for various ages of the system. Due to high concentration of stars, the energy density of the radiation field is

highest at the centre, and the dust temperature attains maximum there. As stellar populations aging, $T_{eq}(r)$ becomes systematically lower in a whole system. As will be mentioned below, this leads to a shift of dust emission toward longer wavelength. At the same time, the temperature gradient becomes flatter, since the effective wavelength of dust heating photons becomes longer. Such photons can travel easier to the outer regions and heat the dust there. However, this flattening of temperature distribution does not affect the SED, significantly.

Figure 12b shows a behaviour of the SED as a function of age. The SED of dust-rich objects is composed of the stellar and dust emissions with the peaks in the UV-NIR and MIR-submm ranges, respectively. Both the stellar and dust emissions decrease as a system aging, because both the emitted UV photons and the absorbed ones by dust become less numerous. When a system is young, the dust emission dominates the SED, while it becomes less important for older ages. Simultaneously, the dust becomes cooler and the dust emission peak shifts from $\sim 40\mu\text{m}$ (for 10 Myr) to $100\mu\text{m}$ (for 10 Gyr). Note that neither the dust absorption nor the dust emission affects the NIR part of SED significantly, while the fraction of energy emitted in FIR decreases monotonically as a system aging. This indicates that the FIR luminosity normalized by the H-band luminosity, L_{FIR}/L_H , is sensitive to age (see also Takagi et al. 1999), where L_{FIR} is the FIR luminosity derived from 60 and 100 μm fluxes.

3.2. The Effect of Optical Depth

Figure 13a shows $T_{eq}(r)$ for different optical depths, τ_V . $T_{eq}(0)$ is almost independent of the optical depth for $\tau_V \leq 40$. When a mean free path of the UV photon is larger than the core radius of stellar distribution, almost all stars in the system can contribute to the heating of dust at the system centre. Note that for the homogeneous distribution of dust the optical depth within $r_{c,S}$ is $10^{2.2}$ times smaller than that defined with r_t in the adopted geometry. The SED of dust emission becomes broader with increasing τ_V , because the temperature at the outer region drops sharply, while $T_{eq}(0)$ is kept constant. This is not true for the case of $\eta \leq 10$. In this case, $T_{eq}(r)$ is less sensitive to τ_V , since strongly concentrated dust obscures the emission from the centre, and the energy density in the outer region is determined by stars in the outer region.

The SEDs with various τ_V are shown in Figure 13b. When τ_V increases, the stellar emission decreases due to the dust absorption, as a result of which the dust emission increases; thus shows a remarkable contrast to the age effect. The fraction of energy emitted in the FIR increases rapidly as a function of τ_V when $\tau_V \ll 1$, but this fraction is less sensitive for $\tau_V \geq 1$. Note that the peak wavelength of dust emission is less sensitive to τ_V than to the age, since only the dust temperature in the outer region depends on τ_V , while the age affects the dust temperature in a whole system.

It is worth noting that the SED approaches the source function for large τ_V ($\gtrsim 10$). In particular, this becomes conspicuous in the UV region, since the extinction cross-section

increases with decreasing λ . Thus, the SED in this region resembles the source function for large τ_V . If stars distribute point-likely and are enshrouded by dust shell, the source function, $S_\lambda^{(1)}$, in dusty medium is zero. Therefore, there should be a sharp cut-off in the SED, i.e. the emission in the UV-NIR spectral region of the population enshrouded by dust is virtually negligible (e.g. Figure 5a in Rowan-Robinson 1980).

3.3. The Effect of Dust Geometry

Figure 14a shows the effect of dust geometry $\eta = r_{c,D}/r_{c,S}$ on $T_{eq}(r)$. $T_{eq}(0)$ drops slightly in the case of $\eta = 1$, since the mean free path of UV photons becomes comparable to $r_{c,S}$. On the other hand, $T_{eq}(r)$ rises as η decreases in the outer region, since the optically thin region from which the UV photons can escape from a system enlarges. However, this effect is rather minor when compared with the effect of age and τ_V .

Figure 14b shows the effect of dust geometry on the SED. The peak of dust emission moves toward shorter wavelength for smaller η , although $T_{eq}(r)$ is not very sensitive to η . This is because the fraction of dust located near the centre where the dust is hottest increases with decreasing η . Note that even if τ_V is the same, the amount of dust changes when η is different. When the dust mass with $\eta = 1000$ is normalized to 1.0, the value of dust mass becomes 0.6, 0.03 and 0.006 for $\eta = 100, 10$ and 1, respectively. Since there is less amount of dust in a system with smaller η , L_{FIR} drops with decreasing η . If the mass of dust is kept constant for different η , then the L_{FIR} is of the same order of magnitude. In the cases of $\eta \ll 100$, the resulting SEDs are close to the intrinsic SED. The bump feature at 2175 Å virtually disappears because the emission from the optically thin region dominates the resulting SED. Even if $\tau_V \gg 1$, the UV-NIR SED does not change significantly. Thus, the observed spread of starburst galaxies in two-colour diagrams can be explained by the stellar and dust distributions only with $\eta \gtrsim 100$ (cf. Gordon et al. 1997). For $\eta \gtrsim 100$, it is difficult to determine the value of η precisely from the SED fitting alone, since the resulting SEDs are degenerate in geometry and optical depth. For instance, the SED of stellar emission with $\eta = 1000$ and $\tau_V = 1$ can be reproduced by the model with $\eta = 100$ and τ_V slightly larger than 1.

3.4. The Effect of System Size

Figures 15a and 15b show $T_{eq}(r)$ and the SEDs for various scaling factors R , respectively. Note that the dust mass varies with R for constant τ_V . The SED of absorbed stellar emission is independent of the physical size of a system, provided that τ_V is kept constant. Since M_\star does not vary, $T_{eq}(r)$ rises as a whole with decreasing R due to the increase of energy density which leads to the shift of peak of dust emission toward shorter wavelength. The distribution of the source function remains the same, since both distributions of stars and dust depend on R in the same way. The scaling relation for absolute value of the source function $S^{(1)}$ is given by $S^{(1)} \propto \varepsilon^*/n\sigma^e$, where $\varepsilon^* \propto R^{-3}$. Since $\tau \propto n\sigma^e R$, we get finally $S^{(1)} \propto R^{-2}/\tau$. Here λ dependence is omitted for clarity. Since the resulting energy density of radiation field and $S^{(1)}$ have the

same dependence on R , the integral in the r.h.s. of the equation (5) is scaled by R^{-2} when the mutual heating of dust is negligible. That integral is proportional to $T_{eq}^{4+\theta}$, if $\sigma_\lambda^a \propto \lambda^{-\theta}$. Thus, $T_{eq}(r)$ is roughly scaled by $R^{-2/(4+\theta)}$.

The effect of R on the peak wavelength of dust emission is comparable to that of the age. Once the age and τ_V are fixed, R could be determined by the peak wavelength of dust emission. This point is important since the results of SED fitting can be restricted by the size of the system derived from the observation. Thus, it can help to determine the dust geometry in the objects with $\tau_V \ll 1$, like elliptical galaxies (see §4.3).

3.5. The Effect of Extinction Curve

Figures 16a and 16b show $T_{eq}(r)$ and the SEDs for the MW, LMC and SMC extinction curve, respectively. In order to enlarge differences among the SEDs, $\tau_V = 30$ is adopted, instead of the standard value. The systematic difference in $T_{eq}(r)$ should be noted, due to the different strength of self-absorption indicated by the depth of the silicate absorption feature at $9.7 \mu\text{m}$. The resulting shift of the peak of dust emission, however, is negligible in comparison with those due to age or R . Although the same τ_V is adopted for the cases of all extinction curves, the resulting luminosity at V band is different because of the different amount of scattered light.

3.6. The Fraction of Absorbed Energy

We introduce the energy fraction absorbed by dust, $\Delta E/E$. The resulting SEDs are integrated from 91.2 nm to $3 \mu\text{m}$ to calculate the amount of unabsorbed energy, E_* , and then $\Delta E/E$ is calculated by using the total energy, E , and $\Delta E = E - E_*$. In Figure 17 and Table 4, $\Delta E/E$ is presented for various ages, τ_V , η , and extinction curves. Note that $\Delta E/E$ is independent of R and is equal to the energy fraction emitted by dust. The dust distributed with larger η absorbs the energy more efficiently. This is due to an increase of the effective amount of dust surrounding the concentrating stars. For the constant value of τ_V and η , $\Delta E/E$ is always larger in younger system, since the absorbed UV photons are more abundant. The dependence on the extinction curve is negligible except for the cases of youngest age 10 Myr and $\tau_V \leq 1$. $\Delta E/E$ increases rapidly as a function of τ_V when $\tau_V \leq 1$. This strong dependence becomes less pronounced for an old system. When $\tau_V \geq 1$, $\Delta E/E$ becomes more sensitive to the age rather than τ_V , especially for young system.

3.7. Summary of Sensitivity Analysis

We summarize the main results of our analysis: 1) the geometry of starburst galaxies should be described by $\eta \gtrsim 100$, since the SED of absorbed stellar emission cannot be red enough to reproduce observed SEDs for $\eta \ll 100$. 2) the UV-NIR SED is most sensitive to the stellar age and optical depth τ_V when $\eta \gtrsim 100$, 3) the FIR excess defined as L_{FIR}/L_H is sensitive to the age but not to τ_V when $\tau_V \geq 1$, which makes it useful for estimating the age of system independently of τ_V , 4) the dust emission reaches maximum at the FIR-submm region,

and the peak wavelength of dust emission depends mainly on the age and R . From this study, we conclude that one can roughly estimate the stellar age from L_{FIR}/L_H , τ_V from the shape of the UV-NIR SED, and R from the peak wavelength of dust emission. The depth of silicate absorption feature at $9.7 \mu\text{m}$ is useful to constrain the type of extinction curve. By using the resulting R and the total stellar mass M_* derived from the normalisation of SED, the size of stellar system is calculated, which can be compared with the observed size of the system to disentangle the degeneracy among R , τ_V and η for the optically thin case (see §4.3).

4. Comparison with Observations

The best-fitting SED model to observed data has been sought by trial and error, using the results of sensitivity analysis given in the previous section. The values of χ^2 are calculated for each fit. Although, in the SED fitting procedure, data at the MIR wavelength region are used to constrain τ_V and to choose the plausible extinction curve, we exclude these data from the calculation of χ^2 . This is because the SED at this wavelength region is very sensitive to the adopted optical properties of silicate grains and PAHs, which are still a matter of debate, and therefore cannot be used to judge the goodness of the fit. For each galaxy, we show not only the best-fitting model, but also the near-fitting models, which are helpful to infer the accuracy of derived model parameters.

As it is shown in §3.3, η should be larger than 100 to reproduce the strongly attenuated SEDs of starburst galaxies, although it is difficult to constrain the precise value of η from the SED alone. Here, we adopt $\eta = 1000$ for starburst galaxies, as a result of which the dust geometry is very close to the simple homogeneous distribution. The model parameters to be determined by observed SEDs are the age of stellar populations t , optical depth in V -band, τ_V , and the size scaling factor R . For an elliptical galaxy NGC2768, the SED from UV to NIR is reproduced by a galactic wind model, following Kodama & Arimoto (1997), and then the observed SED of dust emission is used to constrain τ_V , η and R . Thus, actually we fit SEDs of both starburst and elliptical galaxies by employing three free parameters. The resulting parameters for the best-fitting models and the derived quantities are tabulated in Tables 5 and 6, respectively.

4.1. Arp220

Arp220 is the nearest ultraluminous infrared galaxy at a distance 77 Mpc away from the Milky Way (Soifer et al. 1987). Recent observations by ISO suggest that the source of dust heating is nuclear starburst rather than the AGN (Lutz et al. 1996; Lutz, Veilleux & Genzel 1999). Wynn-Williams & Becklin (1993) derived the "compactness" of MIR emission of Arp220. The compactness is defined by the ratio of fluxes observed in two different apertures, $5''.7$ and $100''$. They show that about 99% of MIR emission comes from the region within $5''.7$ aperture. Furthermore, Soifer et al. (1999) observed Arp220 with the Keck II telescope to find

that the $24.5 \mu\text{m}$ flux in the $4''$ diameter is consistent with the flux density at $25 \mu\text{m}$ obtained by IRAS in a rectangular beam, $\sim 1' \times 5'$. Thus, MIR emission of Arp220 is concentrated in the central region. Here, we confront our models to the central area within $5''$ aperture, which corresponds to ~ 2.0 kpc.

The photometric data are taken from Sanders et al. (1988; B, g, r, i), Carico et al. (1990; J, H, K, L), Smith, Aitken & Roche (1989; MIR), Klaas et al. (1997; MIR to FIR), NED (NASA/IPAC Extragalactic Database; IRAS bands) and Rigopoulou, Lawrence & Rowan-Robinson (1996; submm). Recently, Goldader et al. (2002) presented the far-UV (1457 \AA) and near-UV (2364 \AA) observations with HST/STIS. As noted by the authors, these photometric data are problematic because the large angular size of Arp220 is enough to fill the entire field of view of STIS, which results in the highly uncertain flux level of sky. Therefore, these data are not used for the SED fitting, although we show them in the related figures.

In Figures 18a–d, we show 9 SED models in total, consisting of the best-fitting model and 8 near-fitting models. The parameters for these models are tabulated in Table 7 along with the value of reduced χ^2 . The best-fitting model is indicated by solid lines in all the four figures. It is found that the SMC extinction curve is required, in order to fit simultaneously the strong silicate absorption feature at $9.7 \mu\text{m}$ and the UV-NIR SED. Both the models with MW and LMC type extinction curve overestimate the MIR fluxes, when the UV-NIR SED is well fitted. Therefore, we use the SMC extinction curve for all the nine models.

The best-fitting model is giving by $t=30$ Myr, $\tau_V = 40$ and $R = 0.5$ with the SMC extinction curve, from which the bolometric luminosity $L_{bol} = 1.4 \cdot 10^{12} L_\odot$, the total stellar mass $M_* = 4.2 \cdot 10^{10} M_\odot$ and the total dust mass $M_D = 4.8 \cdot 10^8 M_\odot$ are derived. The resulting $R = 0.5$ corresponds to $r_t = 3.2$ kpc; thus, roughly consistent with the adopted aperture size (~ 2.0 kpc). Note that, in order to compare the size of starburst region, we should be more precise for the definition of starburst region; for example, the effective radius observed at some wavelength should be compared with the effective radius of the model at the same wavelength. However, such a detailed comparison of the geometry is not our main purpose of this paper.

The derived value of reduced χ^2 is relatively large even for the best-fitting model. In the case of Arp220 and also M82, a significant contribution to χ^2 comes from only few most deviating photometric data, e.g. at $3.7 \mu\text{m}$ for Arp220 and at $400 \mu\text{m}$ for M82. We would like to stress that the results of further fine-tuning of the SEDs parameters strongly depend on unknown systematic errors of observations performed with various telescopes, detectors and slightly different aperture sizes over a wide wavelength range. Indeed, genuine systematic uncertainties on data are expected. It is virtually impossible to obtain the exactly aperture-matched photometric data from the measurements performed with different aperture sizes and beam profiles for starburst regions whose surface brightness profile depends on the observed wavelengths (e.g. Scoville et al. 2000). Also, note that starburst regions are surrounded by underlying stellar populations with unclear boundaries. Furthermore, the absolute values of

χ^2 depend on the accuracy of statistical errors which were estimated quite inhomogeneously. Therefore, we refer the value of χ^2 only to compare the goodness of fit among the reference models.

The near-fitting models in Figure 18a have the same model parameters as the best-fitting model, but age. Similarly, the different τ_V and R are adopted for the near-fitting models in Figures 18b and 18c, respectively. The effects of age, τ_V and R are somewhat degenerate in this parameter range, especially due to large τ_V ; i.e. 1) the variations of optical-NIR SED due to the age effects are very similar to those due to τ_V , 2) the average temperature of dust is changed by both the age and R effects. On the other hand, the UV luminosity is less sensitive in the range of age, $t=15 - 60$ Myr. This is because the bolometric luminosity is dominated by the UV luminosity, intrinsically. Note that, in this case, the bolometric luminosity is outlined by the FIR observations.

In Figure 18d, we show the best fitting model together with the models of 10 Myr and 300 Myr. Despite the large difference in age, the optical-NIR SEDs become similar by adjusting both τ_V and R . Therefore, the age of stellar populations is to be conservatively determined in the range of 10 - 300 Myr, when there are no constraints on τ_V and R from the other observations.

Once the optical depth is determined independently of the SED, the age can be constrained in the range of 15 - 60 Myr as shown in Figure 18a. In our model, τ_V is well restricted by the silicate absorption feature when $\tau_V \gtrsim 10$. For Arp220, the best-fitting is achieved with $\tau_V = 40$ for $t = 30$ Myr. From the spectroscopic study with ISO, the extinction of $\tau_V \approx 45$ was derived for Arp220 (Sturm et al. 1996; Genzel et al. 1998). The observations of radio recombination lines result in the similar optical depth (Anantharamaiah et al. 2000). These observational results seem to be consistent with our result. However, it is misleading to compare these values directly, since they are derived by assuming the MW extinction curve. Therefore, we compare optical depth at the NIR region, where hydrogen recombination lines were observed by ISO to derive the extinction. In our model for the SMC type extinction curve, $\tau_V = 40$ corresponds to the optical depth at K band, $\tau_K = 2$, while the observed value is $\tau_K = 4.5$. This difference by a factor of 2 is not serious, since the observed optical depths are inferred from the emission lines of ionized gas, whose distribution could be different from that of dust. Calzetti, Kinney & Storchi-Bergmann (1994) suggest that the discrepancy by a factor of 2 is rather typical for starburst galaxies. Considering these results, we suggest that the constraint on age is rather tighter than the conservative case noted above.

Among 9 models, only the oldest model (300 Myr) shown in Figure 18d is marginally consistent with far-UV data, but overestimates near-UV data. Although these data are less reliable as noted above, the observation by HST/STIS actually suggests very low fluxes at these wavelength, even possible uncertainty of the sky level is taken into account. Such a low flux at the far-UV may be due to either the selective extinction around massive stars or to unexpectedly

large anomaly of the extinction curve. When massive and hot stars tend to be embedded in the clouds whose optical depth is considerably larger than the average which we derive, the far-UV light dominated by these stars can easily be overestimated in our model. As for the extinction curve, it seems neither MW, LMC nor SMC extinction curves could be applicable to starburst regions, especially in the far-UV region in which very small grains play dominant role, since the highly energetic environments probably affect the size distribution of dust grains. In order to reconcile the best-fitting model with the observed far- and near-UV fluxes, the extinction should be extremely effective at these wavelengths by an order of magnitude comparing with the SMC extinction curve. These possibilities should be investigated carefully in the future with reliable observations.

4.2. M82

M82 is a nearby starburst galaxy at a distance of 3.3 Mpc. This galaxy shows remarkable activities including the disturbed dusty appearance and evidence for explosive star formation. This may be caused by an interaction with a neighbouring spiral galaxy M81 located at ~ 36 kpc away in projection (Yun, Ho & Lo 1993; Ichikawa et al. 1995). The centre of this galaxy exhibits strong IR emission extending $\sim 30''$ (Telesco & Harper 1980) which coincides with the effective radius of the bulge component (Ichikawa et al. 1995). Thus, we confront our models to the SED of central starburst region within $\sim 30''$ (~ 0.5 kpc).

The photometric data are taken from Johnson (1966; U, B, V, R, I), Ichikawa et al. (1995, J, H, K), Rice et al. (1988; IRAS bands), Telesco & Harper (1980; FIR), Jaffe, Becklin & Hildebrand (1984; submm), and Elias et al. (1978; submm). The spectrum from $2.4 \mu\text{m}$ to $45 \mu\text{m}$ is obtained with the similar aperture size by the Short Wavelength Spectrometer (SWS) on board the ISO (Sturm et al. 2000). From the ISO-SWS data, we adopt the fluxes at 5, 16, 20, 30, 40 μm for the calculation of χ^2 , at which the continuum emission dominates.

In a similar manner to the case of Arp220, we show the best-fitting model and near-fitting models in Figure 19a-d. The parameters for these models are tabulated in Table 8, along with the resulting values of reduced χ^2 . The best fit is achieved with $t=30$ Myr, $\tau_V=8.5$ and $R=1.0$. We choose the LMC extinction curve for this galaxy, judging from the depth of silicate absorption feature and the goodness of fit to the optical-NIR SED. Using this best-fitting model, we obtain $L_{bol} = 3.7 \cdot 10^{10} L_\odot$, $M_* = 1.1 \cdot 10^9 M_\odot$ and $M_D = 9.0 \cdot 10^6 M_\odot$. The resulting R corresponds to $r_t=1.0$ kpc, which is larger than the observed size of starburst region by a factor of ~ 4 .

The behaviours of SED when changing t , τ_V and R are almost the same as for the case of Arp220. The notable difference is found for the change of τ_V , due to the smaller value of τ_V for M82; i.e. the difference in τ_V affects only the wavelength region shorter than $\sim 2 \mu\text{m}$. For a given age, the uncertainty of τ_V is at most $\Delta\tau_V \sim 2$ as shown in Figure 19b, while $\Delta\tau_V \sim 10$ for Arp220. In the case of no restriction for both age and τ_V , the conservative range of age is

10 – 100 Myr as shown in Figure 19d, which is tighter than in the case of Arp220 due to the smaller value of τ_V .

The observed flux ratio of hydrogen recombination lines ($\text{Pa}\beta/\text{Br}\gamma$) indicates $\tau_K \simeq 1.0$ in the central region (Satyapal et al. 1995). We derive $\tau_K = 0.5$ applying the LMC type extinction curve, and thus find again a factor 2 discrepancy between the optical depth derived from the stellar continuum and the line ratios.

In our model, the optical depth at $9.7\mu\text{m}$ is 1.1 for $\tau_V = 8.5$ with the LMC extinction curve, and therefore the silicate absorption is important. On the contrary, Sturm et al. (2000) concluded that no evidence for the strong $9.7\mu\text{m}$ absorption feature is found. They compared the spectrum of M82 with that of galactic reflection nebula NGC7023 which is expected to be free from the foreground extinction. There is no significant difference in the spectra, except for $\lambda > 12\mu\text{m}$. They succeeded to reproduce the spectrum of M82 up to $\lambda \sim 12\mu\text{m}$ with the scaled spectrum of NGC7023 plus a power-law continuum which starts at $8.5\mu\text{m}$. However, the solution obtained by their model may not be unique, since the effect of self-absorption could be compensated by the assumed flux of power-law continuum, which is a free parameter in their case, but constrained by the other regions of SED in our model.

Thus, it is found that both the SEDs of M82 and Arp220 can be explained by the stellar populations of the same age. We note that, although the derived optical depth is different by a factor of ~ 5 , Arp220 and M82 have the similar mass ratio of dust to stars, ~ 0.01 . This also suggests that both Arp220 and M82 are at the similar evolutionary phase as a starburst galaxy. Therefore, the large difference between their SEDs is mainly caused by the difference in the geometry; i.e. the starburst region of Arp220 is much more compact than that of M82. This argument is consistent with the obtained values of R , which are restricted mainly by the peak wavelength of dust emission; i.e. the average temperature of dust, in other words, the energy density of radiation field and therefore the stellar density.

4.3. HR10

HR10 at $z = 1.44$ is one of famous EROs having $R - K > 6$ in the observed frame (Graham & Dey 1996; Cimatti et al. 1998). In general, extremely red colours are attributed either to very old stellar populations or to young ones heavily obscured by dust (Graham & Dey 1996). The latter case applies for HR10, because of conspicuous dust emission (Dey et al. 1999). The photometric data are all taken from Dey et al. (1999), except for ISO data (Elbaz et al. 2002). For this distant galaxy, a precise choice of aperture for starburst region is difficult, and therefore underlying stellar populations could contribute to the observed fluxes. Dey et al. (1999) note that optical SEDs (in rest frame) is similar to that of nearby ULIRGs rather than that of normal spiral galaxies which is expected for underlying stellar populations in gas-rich galaxies, like HR10. Therefore, we assume that observed fluxes are dominated by starburst stellar populations.

In Figure 20, we show the best-fitting model with the age of 300 Myr, and the near-fitting models with the age of 100 Myr and 1 Gyr. We choose the MW extinction curve which gives better fit to rest frame UV data. The nearest fits are sought by fitting data excluding the MIR data, which are also excluded in the calculation of reduced χ^2 (see Table 9), like in the cases of Arp220 and M82.

For the best-fitting model with $t = 300$ Myr, $\tau_V = 7$ and $R=1.0$, we derive $M_* = 3.3 \cdot 10^{11} M_\odot$ and $L_{bol} = 1.4 \cdot 10^{12} L_\odot$. The absorbed energy corresponds to $\sim 90\%$ of the total one. The dust mass $M_D = 1.2 \cdot 10^9 M_\odot$ is larger than that of the Arp220, despite a smaller τ_V . The resulting R corresponds to $r_t = 18.2$ kpc, while the resolved size of this galaxy is $\sim 0''.9$ (Dey et al. 1999) corresponding to $\sim 5h_{75}^{-1}$ kpc.

For HR10, the acceptable range of age is systematically older than Arp220 and M82. The very red SED of HR10 at UV-optical cannot be reproduced by the model with $t < 100$ Myr. The resulting mass ratio of dust to stars is smaller than that of Arp220 and M82 by a factor of 2. This is consistent with the old age of HR10 as a starburst; i.e. gas, the fuel of starburst, decreases with aging, while stellar mass increases as a result of star formation.

The SED without MIR data can be reproduced with the wide range of starburst age (100 Myr – 1 Gyr) as shown in the figure. However, the oldest model is strongly rejected by MIR data. Note that, for most of starburst galaxies at high redshifts like those found by the submillimetre common-user bolometer array (SCUBA) survey, MIR data are not available, yet. Also, observations at rest frame NIR and/or at the emission peak of dust are extremely important for the tight constraint on the age of high- z starburst galaxies.

4.4. NGC2768

NGC2768, an elliptical galaxy (E6) at a distance of 21.5 Mpc, is one of a few ellipticals that were detected in submm wavelength (Wiklind & Henkel 1995). Photometric data are taken from Longo, Capaccioli & Ceriello (1991; far-UV), RC3 catalogue (de Vaucouleurs et al. 1991; UBV), Frogel et al. (1978; JHK), and Wiklind & Henkel (1995; submm). All data are reduced with the aperture (A) of total diameter (D) of the galaxy, i.e. $A/D=1$. Although Frogel et al. (1978) gave JHK data for $A/D = 1$, the aperture correction they adopted is not consistent with the optical photometry. Therefore, we have adjusted JHK data to the system of the optical data. In the far-UV bands, only the central part of galaxy was observed by the IUE satellite (Longo et al. 1991). Since the far-UV observations are performed in rectangular apertures $10'' \times 20''$, we convert them to the effective circular apertures. We have to note that such procedure is rather uncertain unless a true far-UV photometric profile of the galaxy is known.

Since it is obvious that the stellar population in an elliptical galaxy is by no means the SSP, we calculate the unabsorbed SED of NGC2768 by using a galactic wind model that takes into account a realistic star formation history in a galaxy (Arimoto & Yoshii 1987; Kodama &

Arimoto 1997). Model parameters are the same as Kodama & Arimoto (1997) who explained the empirical colour-magnitude relation of ellipticals in Coma cluster as a sequence of mean stellar metallicity; i.e. $t = 12$ Gyr, $t_{SF} = 0.1$ Gyr, $t_{in} = 0.1$ Gyr and $x = 1.1$, where t is a galactic age, t_{SF} is a time scale of star formation, t_{in} is a time scale of gas infall, and x is a slope of the Salpeter-like IMF for the stellar mass interval $0.10 \leq m/M_{\odot} \leq 60$. NGC2768 has $M_V = -21.8$ mag, from which we derive $t_{gw} = 0.24$ Gyr for an epoch of galactic wind¹.

Figure 21 shows the best-fitting models for NGC2768. Best fits are achieved for $(\tau_V, \eta, R) = (0.3, 1, 12)$ and $(0.035, 1000, 0.7)$ as tabulated in Table 10 with the value of reduced χ^2 . Although we choose the MW extinction curve, the resulting SEDs are not sensitive to the extinction curve, since the amount of reddening required is very small. Obviously, the fit is not unique as the value of χ^2 suggests, because the SEDs from optical to NIR are insensitive to dust in the case of $\tau_V < 1$. The degeneracy can be resolved if one takes into account an observed size of the galaxy. The effective radius of NGC2768 is $r_e = 76''.5$ which corresponds to ~ 8 kpc (Peletier et al. 1990). Using the ratio $r_e/r_c \sim 10$ given by the adopted density distribution of stars, we obtain $r_e = 0.88$ and 11.0 kpc for $R = 1.0$ and 12 , respectively; each value of R is converted to the real size of galaxy by using $M_* = 2.2 \cdot 10^{11} M_{\odot}$ for $L_{bol} = 9.0 \cdot 10^{10} L_{\odot}$. Thus, the model with $R = 12$ and $\eta = 1$ fits better to the observation, giving $M_D = 2.9 \cdot 10^6 M_{\odot}$.

If all the dust in NGC2768 comes from stars via stellar wind, the amount of dust may be given as $M_D = \delta Z M_g$, where δ is dust-to-heavy element ratio, and M_g is the mass of gas. The abundance of gas should be similar to the mean stellar metallicity of a galaxy. Our galactic wind model fitted for NGC2768 gives $[\text{Fe}/\text{H}] = -0.09$, or $\sim 0.80 Z_{\odot}$; thus $Z = 0.016$. After an epoch of galactic wind, the gas has been continuously supplied to the interstellar space from evolving stars, and the amount of gas should become as large as $\sim 20\%$ of total stellar mass (Arimoto 1989). This gives roughly $M_g \simeq 0.2 \times M_* = 4.3 \cdot 10^{10} M_{\odot}$. Therefore, if the dust has always been kept in a galaxy, its amount should be as large as $M_D \sim 2.7 \cdot 10^8 M_{\odot}$ for $\delta = 0.4$. Then the average mass loss rate of dust during 12 Gyr is $\sim 0.02 M_{\odot} \text{ yr}^{-1}$. The amount of dust we derive from the SED fitting is $2.9 \cdot 10^6 M_{\odot}$, which is much smaller than the value expected and corresponds to the amount of dust accumulated during the last ~ 0.1 Gyr. Obviously, most of dust ever ejected from stars was lost to the extragalactic space and/or evaporated.

5. Discussion

5.1. Star formation history of starbursts

In our model, the intrinsic stellar SEDs of the SSP are used. Since galaxies are composed of composite stellar populations, the elapsed time from the onset of starburst, or simply absolute age of starburst can be derived only if the star formation history is known. In the model of Efstathiou et al (2000), the star formation history was parameterized with a time scale for

¹ Kodama & Arimoto (1997) give different wind epoch, since they adopted slightly steeper IMF with $x = 1.2$

an exponential decay of star formation rate, which is estimated from the SED. For M82, they required two bursts of star formation with different time scales (2 Myr and 6 Myr). They derived the starburst ages of 26.5 and 16.5 Myr for each starburst event, respectively. On the other hand, in our model, the SED of M82 can be reproduced with a single starburst population; i.e. no need to assume multiple starburst events, although we derive the age very similar to that derived by Efstathiou et al. (2000). Note that Silva et al. (1998) assumed different star formation history of starbursts as well as the starburst age and applied to M82. This means that the derived star formation history depends on the model assumptions, strongly. Since, at least, these models can reproduce the observed SEDs of M82, we clearly need the other observational constraints, in order to estimate the star formation history of starbursts. The efficiency of star formation which is important clue to the star formation history can be inferred from the ratio of the indicator of star formation rate, such as the bolometric luminosity, to the total mass of gas in the starburst region (Sanders et al. 1988). We suggest that an evolutionary SED model in which the chemical evolution is taken into account, could be helpful to derive the absolute age of starburst, when the observed SED and gas mass are reproduced with the evolutionary SED model, simultaneously.

5.2. *Implications for high redshift starbursts*

Recently, various galaxy populations have been found as candidates of starburst galaxies at high redshifts. These populations can be classified by the wavelength ranges in which galaxy populations are defined; one class consists of galaxies whose characteristics of stellar emission are used as a criterion, such as Lyman-break galaxies and EROs, and for another class dust emission is used, like galaxies detected by ISO and/or SCUBA. It is important to investigate the relationship between these two classes of galaxy population, in order to reveal the nature of high- z starburst galaxies. Lyman-break galaxies are too faint at submm wavelengths to be detected with the currently available telescopes (e.g. Ouchi et al. 1999). EROs have been expected as optical counterparts for SCUBA galaxies, since their extreme red colours can be explained by the significant dust extinction. Although this prospect seems to be confirmed with the submm detection of a prototypical ERO HR10, Cimatti et al. (2002) however found that the star formation rates of star-forming EROs with $R - K > 5$ are an order of magnitude less than those of SCUBA galaxies. This result is consistent with the negative SCUBA detection for $R - K$ EROs. Mohan et al. (2002) detected none of 27 EROs defined with $R - K > 5$ or $I - K > 5$, but one, in the submm wavelengths. Thus, it is not yet clear even whether there is a representative optical/NIR galaxy population for SCUBA galaxies.

Great opportunities to study statistical properties of high- z starburst galaxies will be provided by the future infrared space missions, such as SIRTf-SWIRE (Franceschini et al. 2002) and ASTRO-F (Nakagawa et al. 2001). In both missions, the wide range of wavelength from NIR to FIR will be covered, as a result of which both stellar and dust emission of high- z

starbursts can be observed. Therefore, these missions will be very important to investigate the relationship between the galaxy classes characterized by stellar and dust emissions. Our model is optimal for this analysis, since all regions of SED are physically interrelated, as it was demonstrated for the nearby starburst galaxies. Furthermore, starburst ages, stellar masses and optical depths could be derived for statistical sample of high- z starburst galaxies, as a result of model application to the data obtained with both missions. These results should provide important clues on the process of galaxy formation.

6. Conclusions

We have developed a code which solves the equation of radiative transfer by assuming spherical symmetry for arbitrary radial distributions of stars and dust. Isotropic multiple scattering is assumed and the self-absorption of re-emitted energy from dust is fully taken into account. The adopted dust model takes into account graphite and silicate grains, and PAHs. We successfully reproduce the MW, LMC and SMC type extinction curves as well as the spectra of cirrus emission in the MW.

We adopt the geometry where stars and dust are distributed by the King model. The SEDs of starburst galaxies are reproduced well with the core radius ratio of dust to stars $\eta \geq 100$; thus, dust distributes nearly uniformly and surrounds centrally concentrating stars. The UV-NIR SED is most sensitive to the age and optical depth τ_V . The FIR excess defined by L_{FIR}/L_H depends mainly on age, and is rather insensitive to τ_V when $\tau_V \geq 1$, which allows rough estimate of starburst age by using L_{FIR}/L_H . The peak wavelength of dust emission is in the FIR-submm region, and depends mainly on the age and size scaling factor R . We show that the extinction curve in starburst galaxies is close to that in the SMC (Arp220) or in the LMC (M82), judging from the MIR features when the other parts of SED are reproduced. Therefore, the non-MW type extinction curve should be considered, in order to model the SEDs of starburst galaxies.

UV-submm SEDs of starburst galaxies, Arp220, M82 and HR10, can be reproduced consistently with the reddened starburst stellar populations. The derived age of stellar population in the starburst region of Arp220 is 30 Myr for an instantaneous starburst (SSP model). Although the same age is derived for M82, the obtained optical depth is significantly different ($\tau_V = 8.5$ for M82, and 40 for Arp220). The restriction to the starburst age of M82 is tighter than that of Arp220, due to the smaller optical depth. For prototypical star-forming ERO HR10, we derive systematically older age (300 Myr) than Arp220 and M82, which is required to reproduce the extremely red colour at optical-NIR region. This difference in evolutionary phase as a starburst

is also suggested by the smaller mass ratio of dust to stars in HR10 than that of Arp220 and M82.

The optically thin limit is studied in case of the elliptical galaxy NGC2768, where τ_V ,

galaxy size, and η are degenerate. Determination of the galactic size from observation is required to disentangle this degeneracy. From the observed size and SED of this galaxy, the distribution of dust is found to be similar to that of stars.

T.T. would like to thank T. Shibazaki and late R. Hoshi for their continuous support and fruitful discussions. V.V. are grateful to National Astronomical Observatory of Japan for hospitality during his stay as the guest professor during which a part of work was done. This work was financially supported in part by a Grant-in-Aid for Scientific Research (No. 1164032) by the Japanese Ministry of Education, Culture, Sports and Science, and by a Grant of the Lithuanian State Science and Studies Foundation. This research has made use of the NASA/IPAC Extragalactic Database (NED) which is operated by the Jet Propulsion Laboratory, California Institute of Technology, under contract with the National Aeronautics and Space Administration.

References

- Anantharamaiah K.R., Vaillifond F., Mohan N.R., Goss W.M., Zhao J.H. 2000, *ApJ*, 537, 613
- Arimoto N. 1989, in *Evolutionary Phenomena in Galaxies*, eds. J.E. Beckman, B.E.J. Pagel (Cambridge University Press) p. 323
- Arimoto N., Yoshii Y. 1986, *A&A*, 164, 260
- Arimoto N., Yoshii Y. 1987, *A&A*, 173, 23
- Band D.L., Grindlay J.E. 1985, *ApJ*, 298, 128
- Bithell M., Rees M.J. 1990, *MNRAS*, 242, 570
- Boulanger F., Boissel P., Cesarsky D., Ryter C. 1998, *A&A*, 339, 194
- Bressan A., Chiosi C., Fagotto F. 1994, *ApJS*, 94, 63
- Calzetti D., Kinney A.L., Storchi-Bergmann T. 1994, *ApJ*, 429, 582
- Carico D.P., Sanders D.B., Soifer B.T., Matthews K., Neugebauer G. 1988, *AJ*, 95, 356
- Carico D.P., Sanders D.B., Soifer B.T., Matthews K., Neugebauer G. 1990, *AJ*, 100, 70
- Chambers K.C., Charlot S. 1990, *ApJ*, 348, L1
- Chambers K.C., Miley G.K., van Breugel W.J.M. 1990, *ApJ*, 363, 21
- Chan K.-W., Roellig T.L., Onaka T., Mizutani M., Okumura K., Yamamura I., Tanabé T., Shibai H. et al. 2001, *ApJ*, 546, 273
- Cimatti A., Andreani P., Röttgering H., Tilanus R. 1998, *Nature*, 392, 895
- Cimatti A., Daddi E., Mignoli M., Pozzetti L., Renzini A., Zamorani G., Broadhurst T., Fontana A. et al. 2002, *A&A*, 381, L68
- Combes F., Boissé P., Mazure A., Blanchard A. 1995, in *Galaxies and Cosmology* (Springer-Verlag, Berlin Heidelberg) p. 96
- Désert F.-X., Boulanger F., Puget J.L. 1990, *A&A*, 237, 215
- Désert F.-X., Boulanger F., Shore S.N. 1986, *A&A*, 160, 295
- Devriendt J.E.G., Guiderdoni B., Sadat R. 1999, *A&A*, 350, 381
- de Vaucouleurs G., de Vaucouleurs A., Corwin H.G.Jr., Buta R., Paturel G., Fouque P. 1991, in *The Third Reference Catalogue of Bright Galaxies* (Springer Verlag, New York) [RC3]
- Dey A., van Breugel W., Vacca W.D., Antonucci R. 1997, *ApJ*, 490, 698
- Dey A., Graham J.R., Ivison R.J., Smail I., Wright G.S., Liu M.C. 1999, *ApJ*, 519, 610
- Draine B.T., Anderson N. 1985, *ApJ*, 292, 494
- Draine B.T., Lee H.M. 1984, *ApJ*, 285, 89
- Dwek E. 1986, *ApJ*, 302, 363
- Dwek E., Arendt R. G., Fixsen D. J., Sodroski T. J., Odegard N., Weiland J. L., Reach W. T., Hauser, M. G. et al. 1997, *ApJ*, 475, 565
- Eales S.A., Rawlings S., Dickinson M., Spinrad H., Hill G.J., Lacy M. *ApJ*, 1993, 409, 578
- Elbaz D., Flores H., Chantal P., Mirabel I.F., Sanders D., P.-A. Duc, Cesarsky C.J., Aussel H. 2002, *A&A*, 381, L1

Efstathiou A., Rowan-Robinson M., Siebenmorgen R. 2000, MNRAS, 313, 734

Eisenhardt P., Dickinson M. 1992, ApJ, 399, L47

Elias J.H., Ennis D.J., Gezari D.Y., Hauser M.G., Houck J.R., Lo K.Y., Matthews K., Nadeau D. et al. 1978, ApJ, 220, 25

Fagotto F., Bressan A., Bertelli G., Chiosi C. 1994a, A&AS, 104, 365

Fagotto F., Bressan A., Bertelli G., Chiosi C. 1994b, A&AS, 105, 29

Fioc M., Rocca-Volmerange B. 1997, A&A, 326, 950

Franceschini A., Lonsdale C., SWIRE Co-Investigator Team 2002, astro-ph/0202463

Frogel J.A., Persson S.E., Aaronson M., Matthews K. 1978, ApJ, 220, 75

Genzel R., Lutz D., Sturm E., Egami E., Kunze D., Moorwood A.F.M., Rigopoulou D., Spoon H.W.W. et al. 1998, A&A, 498, 579

Goldader J.D., Joseph R.D., Doyon R., Sanders D.B. 1995, ApJ, 444, 97

Goldader J.D., Meurer G., Heckman T.M., Seibert M., Sanders D.B., Calzetti D., Steidel C.C. 2002, ApJ, 568, 651

Gordon K.D., Calzetti D., Witt A.N. 1997, ApJ, 487, 625

Graham J.R., Dey A. 1996, ApJ, 471, 720

Graham J.R., Matthews K., Soifer B.T., Nelson J.E., Harrison W., Jernigan J.G., Lin S. et al. 1994, ApJ, 420, L5

Guhathakurta P., Draine B.T. 1989, ApJ, 345, 230

Gunn J.E., Stryker L.L. 1983, ApJS, 52, 121

Ichikawa T., Yanagisawa K., Itoh N., Tarusawa K., van Driel W., Ueno M. 1995, AJ, 109, 2038

Ivezić Ž., Groenewegen M.A.T., Men'shchikov A., Szczerba R. 1997, MNRAS, 291, 121

Jaffe D.T., Becklin E.E., Hildebrand R.H. 1984, ApJ, 285, L31

Johnson H.L. 1966, ApJ, 143, 187

Klaas U., Haas M., Heinrichsen I., Schulz B. 1997, A&A, 325, L21

Kobayashi Y., Sato S., Yamashita T., Shiba H., Takami H. 1993, ApJ, 404, 94

Kodama T., Arimoto N. 1997, A&A, 320, 41

Kurucz R.L. 1992, The stellar Population of Galaxies, eds. B. Barbuy, A. Renzini (Dordrecht: Kluwer), p. 225

Lacy M., Rawlings S. 1996, MNRAS, 280, 888

Laor A., Draine B.T. 1993, ApJ, 402, 441

Léger A., d'Hendecourt L., Défourneau D. 1989, A&A, 216, 148

Leitherer C., Heckman T.M. 1995, ApJS, 96, 9

Lemke D., Mattila K., Lehtinen K., Laureijs R. J., Liljestrom T., Léger, A., Herbstmeier U. 1998, A&A, 331, 742

Lilly S.J. 1988, ApJ, 333, 161

Longo G., Capaccioli M., Ceriello A. 1991, A&AS, 90, 375

Low F.J., Young E., Beintema D.A., Gautier T.N., Beichman C.A., Aumann H.H., Gillett F.C., Neugebauer G. et al. 1984, ApJ, 278, L14

Lutz D., Genzel R., Sternberg A., Netzer H., Kunze D., Rigopoulou D., Strum E., Egami E. et al. 1996, A&A, 315, L137

Lutz D., Veilleux S., Genzel R. 1999, ApJ, 517, L13

Mathis J.S. 1990, ARA&A, 28, 37

Mathis J.S., Mezger P.G., Panagia N. 1983, A&A, 128, 212

Mathis J.S., Rimpl W., Nordsieck K.H. 1977, ApJ, 217, 425

Mazzei P., De Zotti G., Xu C. 1994, ApJ, 422, 81

Meurer G.R., Heckman T.M., Lehnert M.D., Leitherer C., Lowenthal J., 1997, AJ, 114, 54

Meurer G.R., Heckman T.M., Leitherer C., Kinney A., Robert C., Garnett D.R. 1995, AJ, 110, 2665

Mihalas D. 1978, Stellar Atmospheres (W.H. Freeman and Company, San Francisco), ch. 2

Mohan N.R., Cimatti A., Rottgering H.J.A., Andreani P., Severgnini P., Tilanus R.P.J., Carilli C.L., Stanford S.A. 2002, A&A, 383, 440

Nakagawa T. 2001, in The promise of Herschel Space Observatory, ed. G.L. Pilbratt, J. Cernicharo, A.M. Heras, T. Prusti, R. Harris, (Noordwijk ESA-SP 460), p.67

O'Connell R.W., Gallagher J.S., Hunter D.A. 1994, ApJ, 433, 65

Omont A. 1986, A&A, 164, 159

Ouchi M., Yamada T., Kawai H., Ohta K. 1999, ApJ, 517, L19

Pickles A.J. 1985, ApJS, 59, 33

Pei Y.C. 1992, ApJ, 395, 130

Peletier R.F., Davies R.L., Illingworth G.D., Davis L.E., Cawson M. 1990, AJ, 100, 1091

Puget J.L., Léger A. 1989, ARA&A, 27, 161

Rakos K.D., Maindl T.I., Schombert J.M. 1996, ApJ, 466, 122

Rice W., Lonsdale C.J., Soifer B.T., Neugebauer G., Koplan E.L., Lloyd L.A., de Jong T., Habing H., J. 1988, ApJS, 68, 91

Rieke G.H., Lebofsky M.J. 1985, ApJ, 288, 618

Rigopoulou D., Lawrence A., Rowan-Robinson M. 1996, MNRAS, 278, 1049

Rowan-Robinson M. 1980, ApJS, 44, 403

Rowan-Robinson M., Efstathiou A. 1993, MNRAS, 263, 675

Sanders D.B., Soifer B.T., Elias J.H., Madore B.F., Matthews K., Neugebauer G., Scoville N.Z. 1988, ApJ, 325, 74

Satyapal S., Watson D.M., Pipher J.L., Forrest W.J., Coppensbarger D., Raines S.N., Libonate S., Piche F. et al. 1995, ApJ, 448, 611

Schmitt H.R., Kinney A.L., Calzetti D., Bergmann T.S. 1997, AJ, 114, 592

Scoville N.Z., Evans A.S., Thompson R., Reike M., Hines D.C., Low F.J., Dinshaw N., Surace J.A. et al. 2000, AJ, 119, 991

Shioya Y., Taniguchi Y., Trentham N. 2001, MNRAS, 321, 11
Siebenmorgen R., Krügel E. 1992, A&A, 259, 614
Silva L., Granato G.L., Bressan A., Danese L. 1998, ApJ, 509, 103
Smith C.H., Aitken D.K., Roche P.F. 1989, MNRAS, 241, 425
Soifer B.T., Sanders D.B., Madore B.F., Neugebauer G., Danielson D.E., Elias J.H., Lonsdale C.J., Rice W.L. 1987, ApJS, 320, 238
Soifer B.T., Neugebauer G., Matthews K., Becklin E.E., Ressler M., Werner M.W., Weinberger A.J., Egami E. 1999, ApJ, 513, 207
Sturm E., Lutz D., Genzel R., Sternberg A., Egami E., Kunze D., Rigopoulou D., Bauer O.H. et al. 1996, A&A, 315, L133
Sturm E., Lutz D., Tran D., Feuchtgruber H., Genzel R., Kunze D., Moorwood A.F.M., Thornley M. D. 2000, A&A, 358, 481
Takagi T., Arimoto N., Vansvičius V. 1999, ApJ, 523, 107
Telesco C.M., Harper D.A. 1980, ApJ, 235, 392
Tacconi-Garman L.E., Sternberg A., Eckart A. 1996, AJ, 112, 918
Totani T., Takeuchi T.T. 2002, ApJ, 570, 470
VandenBerg D.A., Hartwick F.D.A., Dawson P., Alexander D.R. 1983, ApJ, 266, 747
Verstraete L., Léger A. 1992, A&A, 266, 513
Vansvičius V., Arimoto N., Kodaira K. 1997, ApJ, 474, 623
Vassiliadis E., Wood P.R. 1993, ApJ, 413, 641
Vassiliadis E., Wood P.R. 1994, ApJS, 92, 125
Weingartner J.C., Draine B.T. 2001, ApJS, 134, 263
Wiklind T., Henkel C. 1995, A&A, 297, L71
Windhorst R.A., Burstein D., Mathis D.F., Neuschaefer L.M., Bertola F., Buson L.M., Koo D.C., Matthews K. et al. 1991, ApJ, 380, 362
Witt A.N., Thronson H.A., Capuano J.M. 1992, ApJ, 393, 611
Wynn-Williams C.G., Becklin E.E. 1993, ApJ, 412, 535
Yi S. 1996, Ph.D. Thesis, Yale University
Yun M.S., Ho P.T.P., Lo K.Y. 1993, ApJ, 411, L17

Table 1. Parameters of PAH features

$\lambda[\mu m]$	$\nu_0[cm^{-1}]$	$\Gamma[cm^{-1}]$	$A[10^{-25}cm^3]$
3.3.....	3030	23.5	1.4 N_H
6.2.....	1610	36.5	0.7 N_C
7.7.....	1300	59.0	2.0 N_C
8.6.....	1160	34.5	1.2 N_H
11.3....	885	17.0	14.1 N_H
12.7....	787	32.5	11.1 N_H

Note. N_C and N_H are the number of carbon and hydrogen atoms in a PAH molecule, respectively.

Table 2. The relative fractions of dust particles

	M_D/M_H	Graphite		Silicate		PAH
		BG	VSG	BG	VSG	
MW	$8.0 \cdot 10^{-3}$	0.37	0.08	0.43	0.07	0.05
LMC	$3.6 \cdot 10^{-3}$	0.10	0.02	0.74	0.13	0.01
SMC	$1.9 \cdot 10^{-3}$	0.04	0.009	0.808	0.138	0.005

Note. M_D/M_H is the mass ratio of dust to hydrogen.

Table 3. Parameters of the standard model

Age	τ_V	R	η	Extinction Curve
10 Myr	1.0	1.0	1000	MW

Table 4. Fraction (%) of the absorbed energy

MW Extinction Curve												
τ_V	1^\dagger	10 Myr			1 Gyr				10 Gyr			
		10^\dagger	100^\dagger	1000^\dagger	1	10	100	1000	1	10	100	1000
0.5	6	26	45	49	4	11	18	20	4	9	14	15
1.0	10	39	66	71	5	18	31	34	5	14	24	26
2.0	15	52	83	87	8	29	49	53	7	24	40	44
5.0	23	66	93	96	14	46	74	78	12	40	66	71
10.0....	30	74	97	98	19	58	87	90	17	53	82	86

SMC Extinction Curve												
τ_V	1	10 Myr			1 Gyr				10 Gyr			
		10	100	1000	1	10	100	1000	1	10	100	1000
0.5	8	32	55	59	4	11	19	20	4	9	14	15
1.0	13	45	72	77	6	19	32	34	5	14	24	26
2.0	18	56	84	88	8	29	49	53	7	23	40	43
5.0	26	69	94	96	14	46	73	77	12	40	65	70
10.0....	33	76	97	98	19	57	86	89	17	52	81	85

† Core radius ratio, η

Table 5. Parameters of the best-fitting models

Name	t [Gyr]	τ_V	R	η	Extinction Curve	Reduced χ^2
Arp220	0.03	40	0.5	1000	SMC	1.69
M82	0.03	8.5	1.0	1000	LMC	1.85
HR10	0.3	7.0	1.0	1000	MW	1.64
NGC2768	12^a	0.3	12.	1	MW ^a	1.67

^a assumed parameters

Table 6. Derived galaxy luminosities and masses

Name	M_*	L_{bol}	M_D
	$[10^{11} M_\odot]$	$[10^{11} L_\odot]$	$[10^7 M_\odot]$
Arp220	0.42	14.	48.
M82	0.011	0.37	0.90
HR10	3.3	14.	120.
NGC2768	2.2	0.9	0.29

Table 7. Model parameters for Arp220

Name	t [Myr]	τ_V	R	η	Extinction curve	Reduced χ^2
model 1	30	40	0.5	1000	SMC	1.69
model 2	15	40	0.5	1000	SMC	2.94
model 3	60	40	0.5	1000	SMC	5.37
model 4	30	60	0.5	1000	SMC	2.34
model 5	30	30	0.5	1000	SMC	4.63
model 6	30	40	0.3	1000	SMC	3.62
model 7	30	40	1.0	1000	SMC	2.74
model 8	300	70	0.1	1000	SMC	3.06
model 9	10	30	1.0	1000	SMC	3.98

Table 8. Model parameters for M82

Name	t [Myr]	τ_V	R	η	Extinction curve	Reduced χ^2
model 1	30	8.5	1.0	1000	LMC	1.85
model 2	15	8.5	1.0	1000	LMC	3.35
model 3	60	8.5	1.0	1000	LMC	8.83
model 4	30	10.	1.0	1000	LMC	2.51
model 5	30	7.0	1.0	1000	LMC	2.64
model 6	30	8.5	1.5	1000	LMC	6.95
model 7	30	8.5	0.5	1000	LMC	3.75
model 8	10	8.0	0.1	1000	LMC	2.72
model 9	100	10.	1.0	1000	LMC	3.72

Table 9. Model parameters for HR10

Name	t [Myr]	τ_V	R	η	Extinction curve	Reduced χ^2
model 1	300	7.0	1.0	1000	MW	1.67
model 2	100	5.0	3.0	1000	MW	3.59
model 3	1000	20.	0.1	1000	MW	2.08

Table 10. Model parameters for NGC2768

Name	t [Gyr]	τ_V	R	η	Extinction curve	Reduced χ^2
model 1	12^a	0.3	12	1	MW ^a	1.64
model 2	12^a	0.035	0.7	1000	MW ^a	1.69

^a assumed parameters

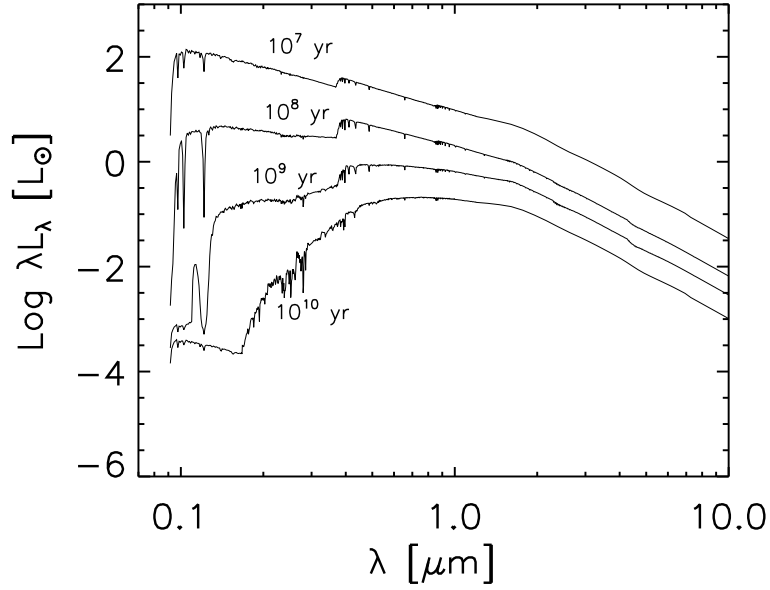


Fig. 1. The spectral energy distributions (SEDs) of the simple stellar populations (SSP) (Kodama & Arimoto 1997) are given for ages: 10 Myr (top), 100 Myr, 1 Gyr, and 10 Gyr (bottom). The luminosity is given for the SSP with the initial mass (i.e. mass at zero age) of $1 M_{\odot}$.

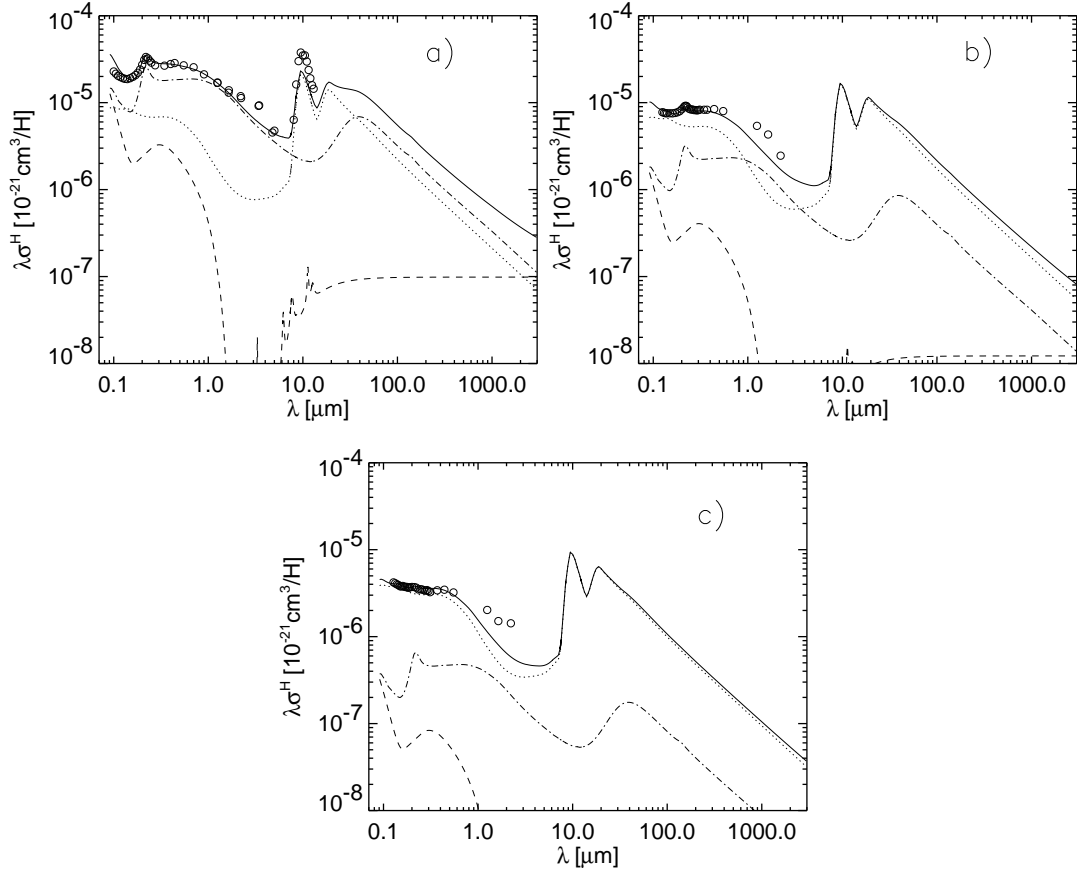


Fig. 2. The MW, LMC and SMC type extinction curves per hydrogen atom are shown in panel a), b) and c), respectively. The dot-dashed curve is for graphite, dotted for silicate, dashed for PAH, and solid for total extinction. The average extinction curves of each type are taken from Pei (1992) and Rieke & Lebofsky (1985), and are depicted by open circles.

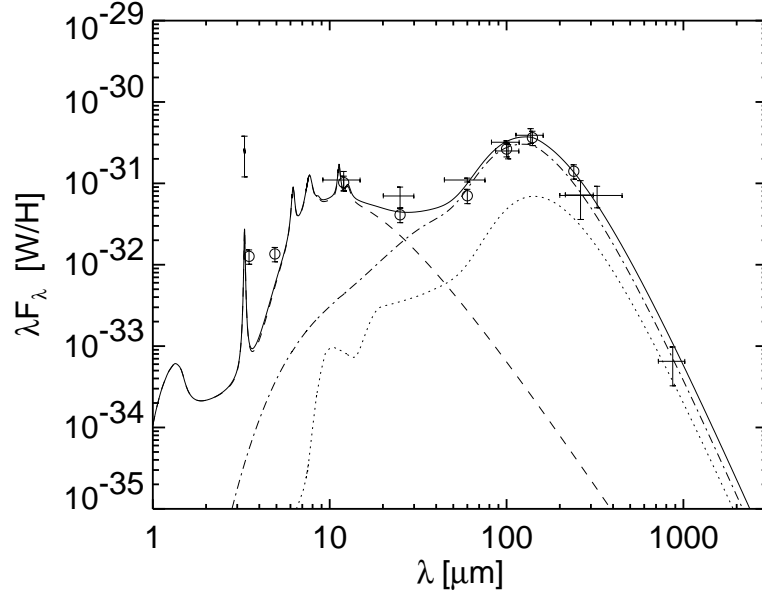


Fig. 3. The spectra of cirrus emission in the MW. The line symbols are the same as in Figure 2. COBE observations are represented by open circles (Dwek et al. 1997). The other data are taken from Désert et al. (1990) and references therein.

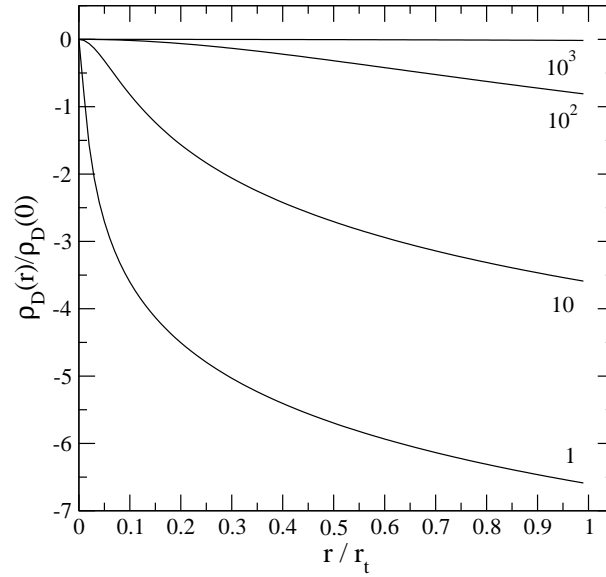


Fig. 4. The normalized dust density profiles given for various η values. The horizontal axis is normalized by r_t ($=r_{t,S}$).

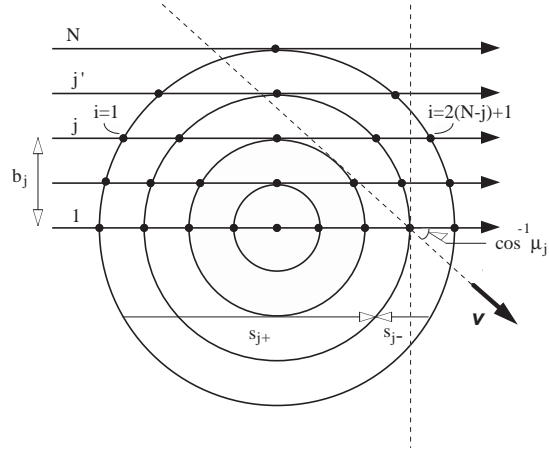


Fig. 5. Scheme of dusty galaxy. The intensity is calculated and stored at the positions of filled circles. b_j indicates the impact parameter for the j -th ray. The angular integration at $r_{j'}$, where $j' = j + 1$, is performed by using the rays depicted by dashed lines and that with $j = 1$. The cosine grid μ_j at $r_{j'}$ is defined by \mathbf{v} and a radius vector.

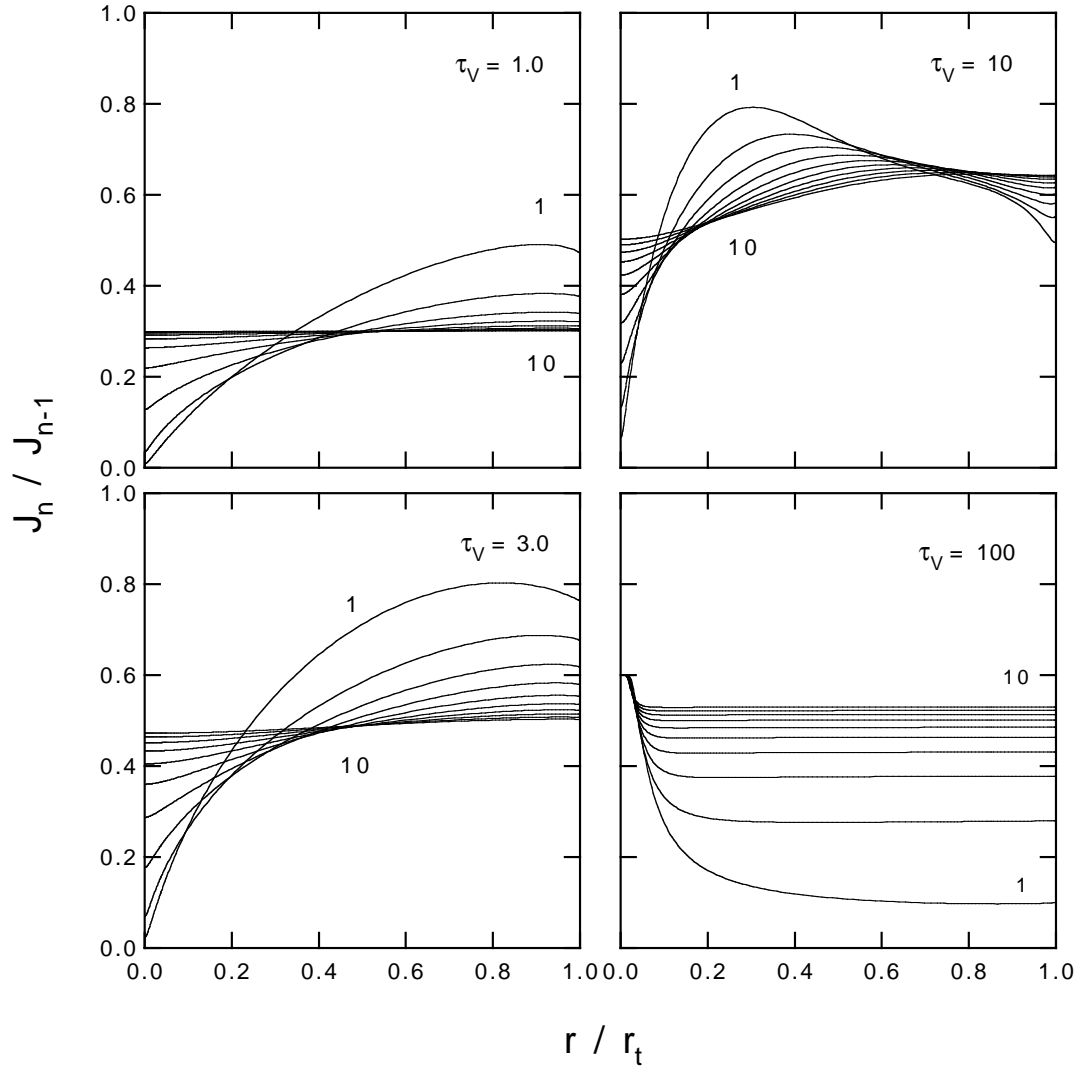


Fig. 6. A mean intensity ratio of scattering terms J_n/J_{n-1} , where J_n and J_{n-1} are n and $n - 1$ times scattered light, respectively. The adopted parameters are $\eta = 1000$, $\tau_V = 1.0, 3.0, 10, 100$, and $n = 1$ to 10 with $\Delta n = 1$.

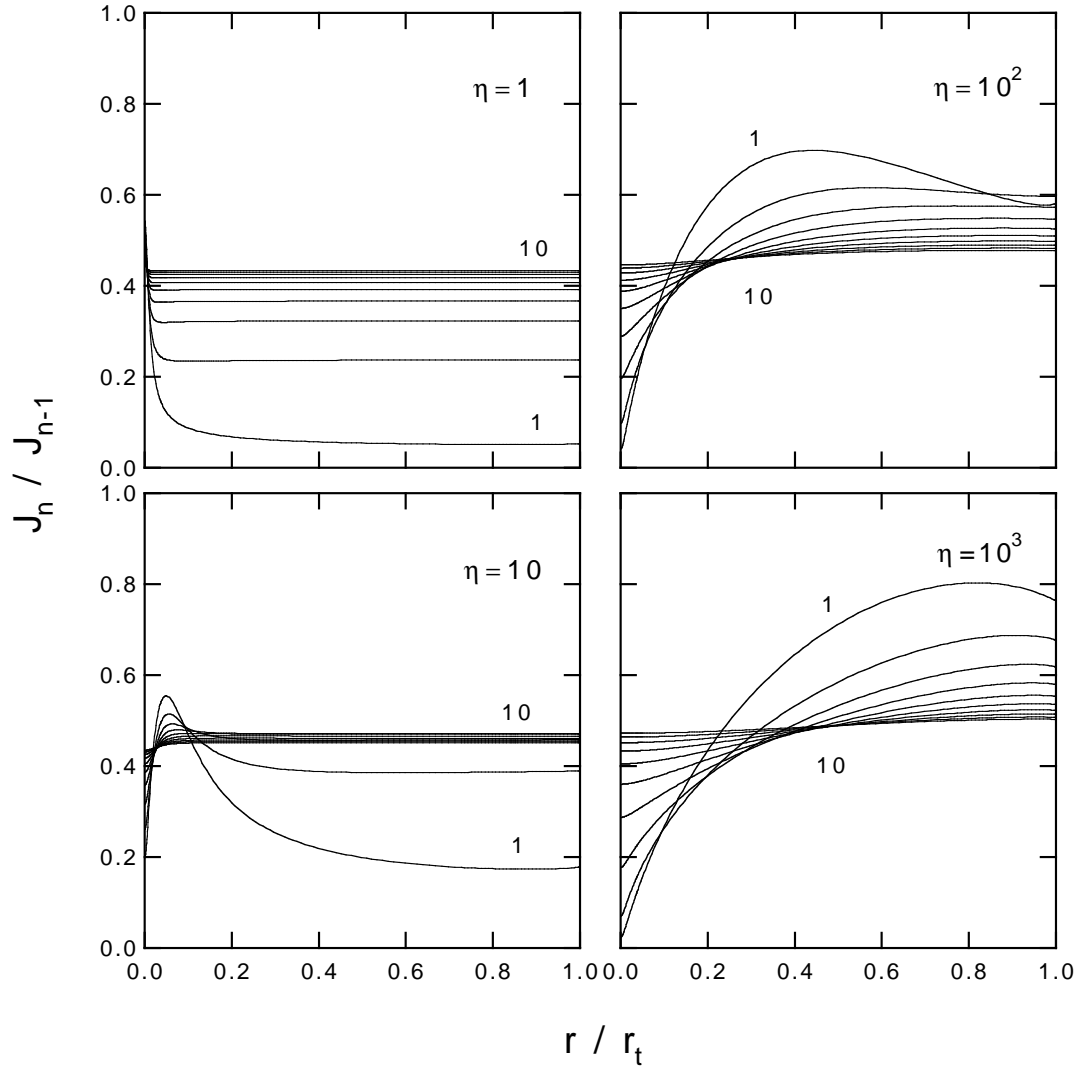


Fig. 7. The same as in Figure 6, but for $\tau_V = 3.0$. The adopted parameter $\eta = 1, 10, 100, 1000$ is indicated at the upper-right corner of each panel.

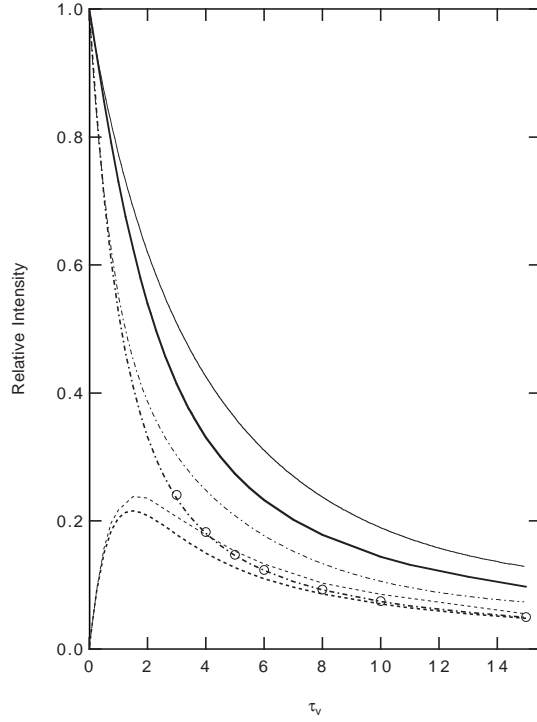


Fig. 8. The fraction of light which escapes from a dust-rich galaxy. Stars and dust are assumed to distribute homogeneously in this case. We adopt $\omega = 0.6$. The thick lines indicate the results of present model, while the thin lines are taken from Witt et al. (1992). Solid, dot-dashed, and dotted lines show the total light, the direct stellar light, and the scattered light, respectively. The analytical solution for the direct stellar light is shown by open circles.

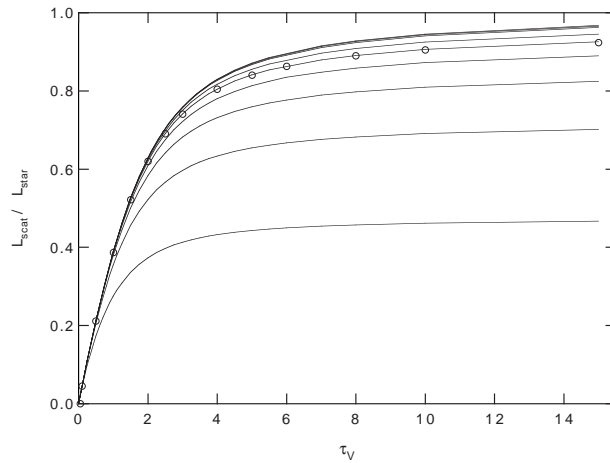


Fig. 9. The ratio of scattered light to the direct stellar light as a function of τ_V for different number of the scattering terms $n = 1$ (bottom) to $n = 10$ (top) with $\Delta n = 1$. Note that lines for $n \geq 7$ are nearly identical. The results of Witt et al. (1992) are plotted as open circles.

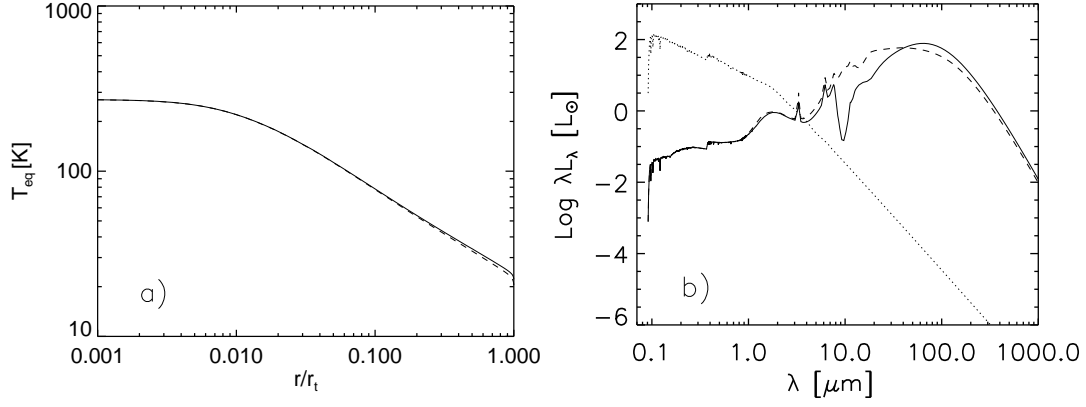


Fig. 10. The effects of self-absorption. (a) The temperature distributions of graphite BG with $a = 0.15 \mu\text{m}$. The solid and dashed lines indicate $T_{eq}(r)$ with and without the self-absorption, respectively. (b) The SEDs. The solid and dashed lines indicate λL_λ with and without the self-absorption, respectively. The dotted line gives the intrinsic SED. The adopted parameters are $\eta = 1000$, $\tau_V = 30.0$, $t = 10$ Myr, and the SMC extinction curve.

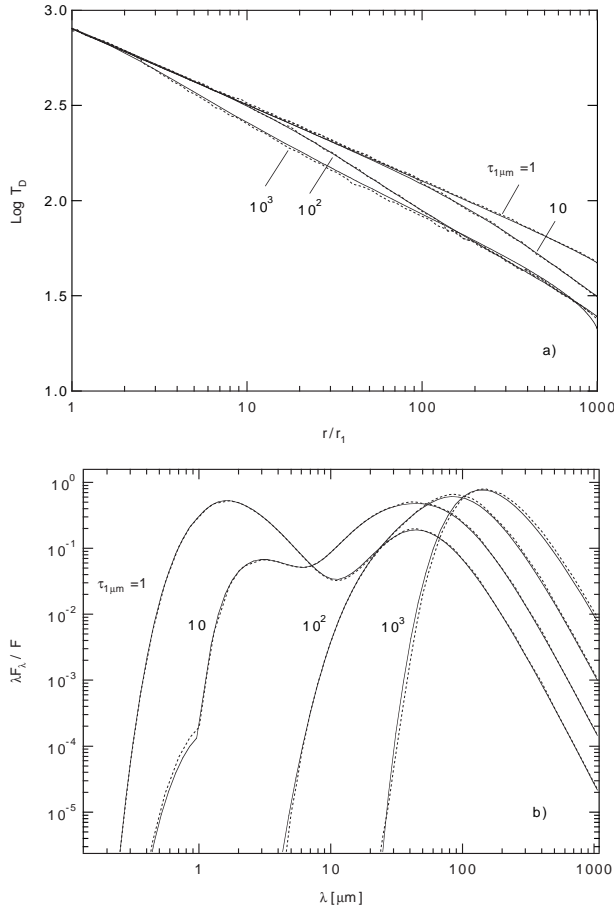


Fig. 11. A comparison with output of DUSTY code by Ivezić et al. (1997). Solid and dotted lines indicate the results of present model and those of Ivezić et al., respectively. (a) The temperature distribution of dust. The radius is given in units of a radius of central dust free cavity, r_1 . (b) The SEDs normalized by an integrated flux, F .

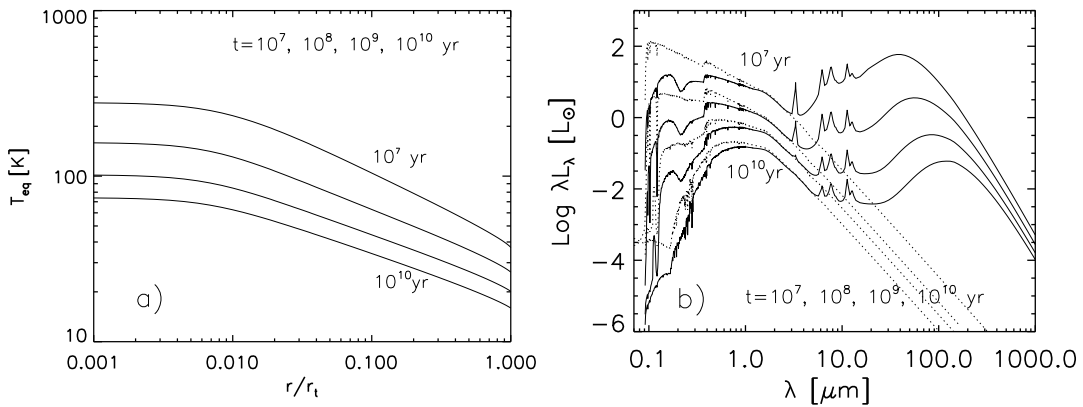


Fig. 12. The effects of age. Parameters, except for the age, are the same as for the standard model (see text). (a) The temperature distribution of graphite BG with $a = 0.15 \mu\text{m}$ for 10 Myr, 100 Myr, 1 Gyr, and 10 Gyr old. (b) The same as (a), but for the SEDs. Dotted lines give the intrinsic SEDs.

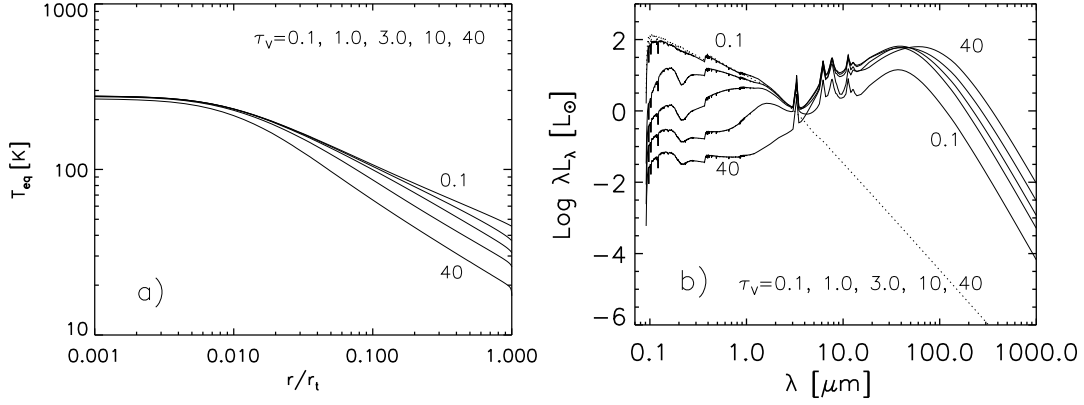


Fig. 13. The effects of optical depth. Parameters, except for τ_V , are the same as for the standard model (see text). (a) The temperature distribution of graphite BG with $a = 0.15 \mu\text{m}$ for $\tau_V = 0.1$ (top), 1.0, 3.0, 10 and 40 (bottom). (b) The same as (a), but for the SEDs. The dotted line shows the intrinsic SED.

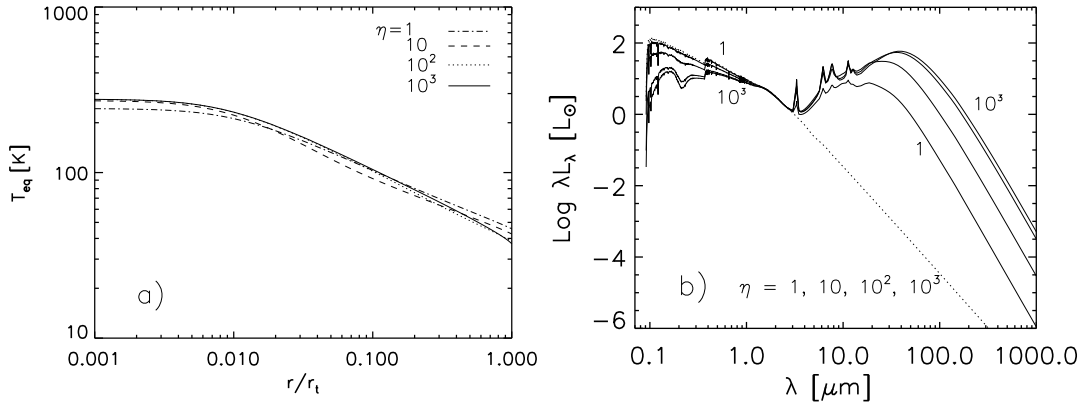


Fig. 14. The effects of dust geometry. Parameters, except for η , are the same as for the standard model (see text). (a) The temperature distribution of graphite BG with $a = 0.15 \mu\text{m}$ for $\eta = 1$ (dot-dashed line), 10 (dashed line), 100 (dotted line), and 1000 (solid line). (b) The same as (a), but for the SEDs. The dotted line shows the intrinsic SED. Figures indicate η values which increase from top to bottom for the stellar emission, but from bottom to top in FIR-submm range.

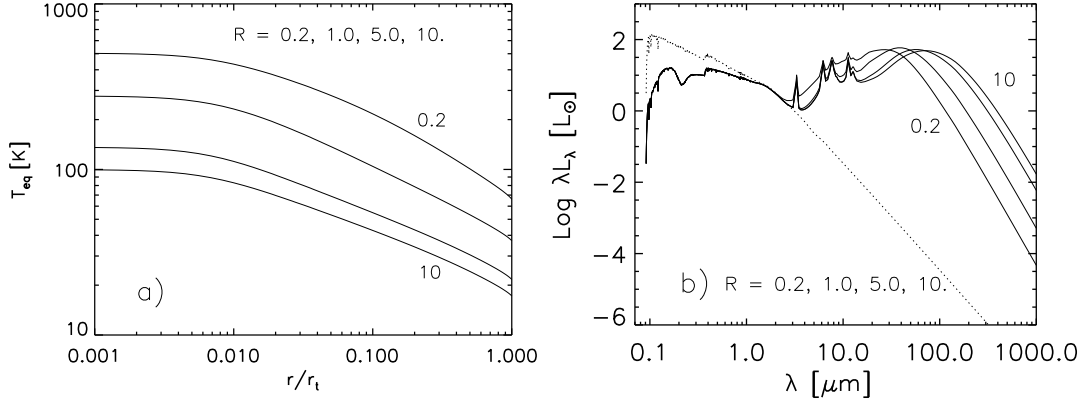


Fig. 15. The effects of system size. Parameters, except for R , are the same as for the standard model (see text). (a) The temperature distribution of graphite BG with $a = 0.15 \mu\text{m}$ for $R = 0.2$ (top), 1.0, 5.0 and 10.0 (bottom). (b) The same as (a), but for the SEDs. The dotted line indicates the intrinsic SED.

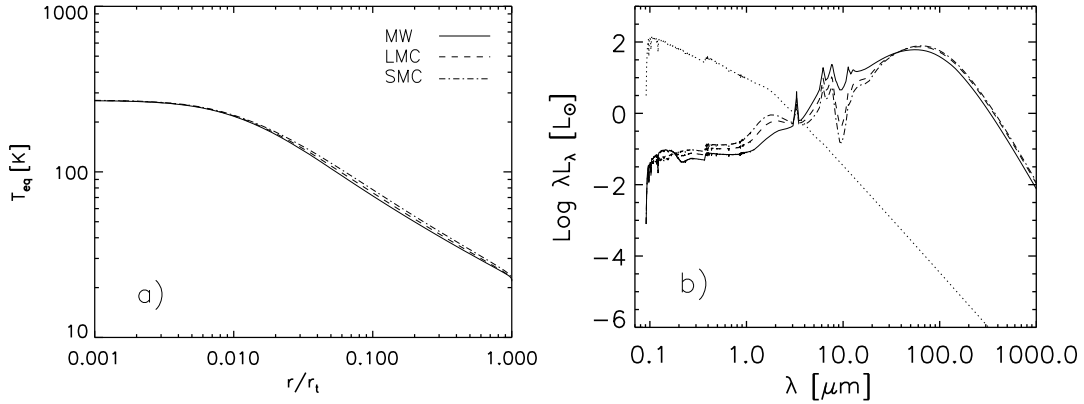


Fig. 16. The effects of extinction curve. Parameters, except for $\tau_V = 30$ and the extinction curve, are the same as for the standard model (see text). (a) The temperature distribution of graphite BG with $a = 0.15 \mu\text{m}$ for the MW (solid line), the LMC (dashed line), and the SMC (dot-dashed line) extinction curves. (b) The same as (a), but for the SEDs. The dotted line indicates the intrinsic SED.

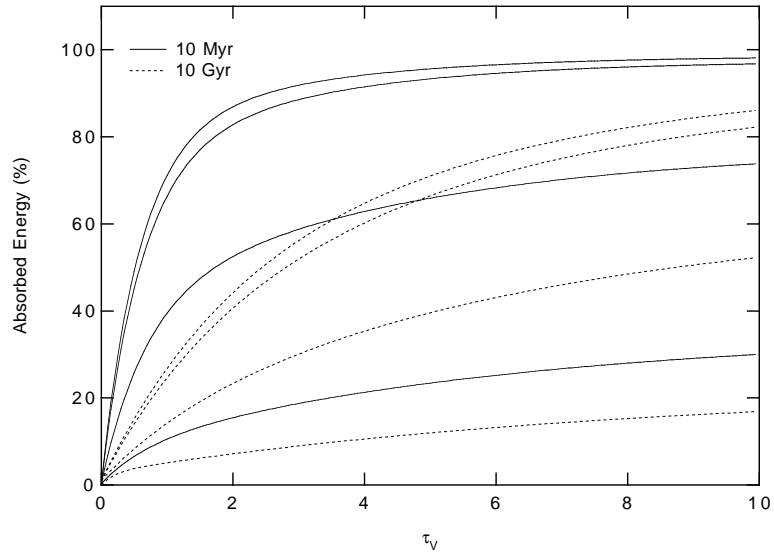


Fig. 17. The absorbed energy fraction as a function of optical depth. Solid and dotted lines correspond to 10 Myr and 10 Gyr, respectively. The four lines for each age correspond to geometry with $\eta = 1$ (bottom), 10, 100, and 1000 (top).

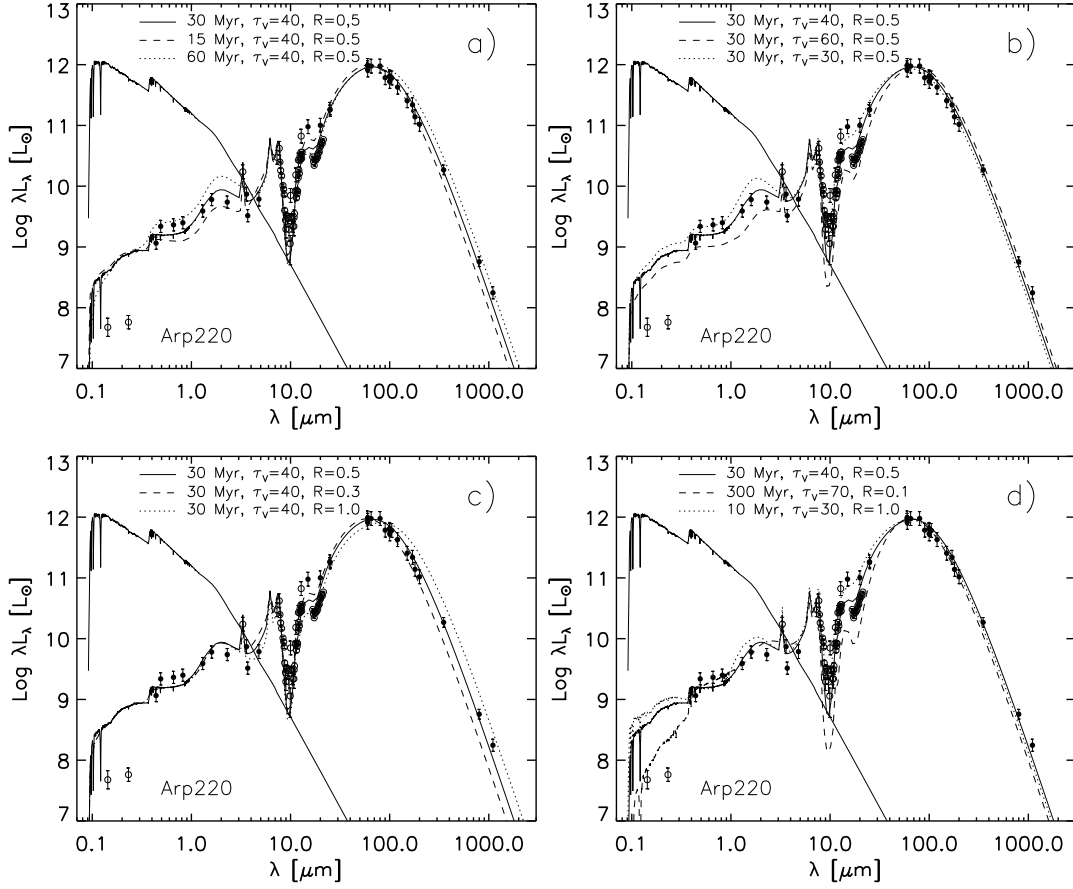


Fig. 18. The results of SED fitting for Arp220. The SMC type extinction curve and $\eta = 1000$ are adopted for all models. The other parameters for each model are denoted in the figure. We use solid circles for data which are used to calculate the value of χ^2 , otherwise open circles are adopted. The upper solid line at UV-NIR region is the intrinsic stellar SED with the age of 30 Myr. In all panels, the best-fitting model is indicated by solid lines. Horizontal axis is the rest frame wavelength. (a) The SED models with the same parameters, but age, as that of best-fitting model indicated by solid line. (b) The same as (a), but τ_V is varied, instead of age. (c) The same as (a), but R is varied, instead of age. (d) The fitting model with the fixed age (10 and 300 Myr), shown with the best-fitting model.

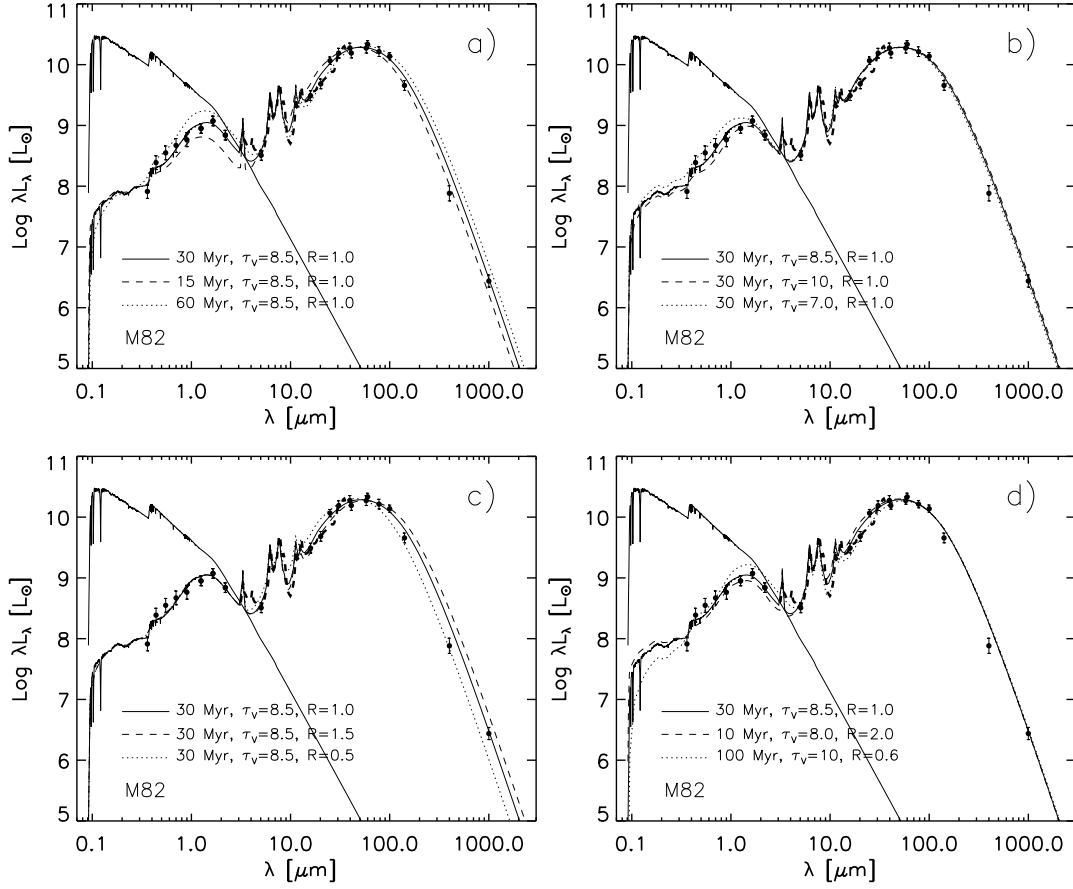


Fig. 19. The same as Figure 19, but for M82. LMC type extinction curve and $\eta = 1000$ are adopted for all models. Thick dashed line is for the ISO-SWS spectrum. The upper solid line at UV-NIR region is the intrinsic stellar SED with the age of 30 Myr.

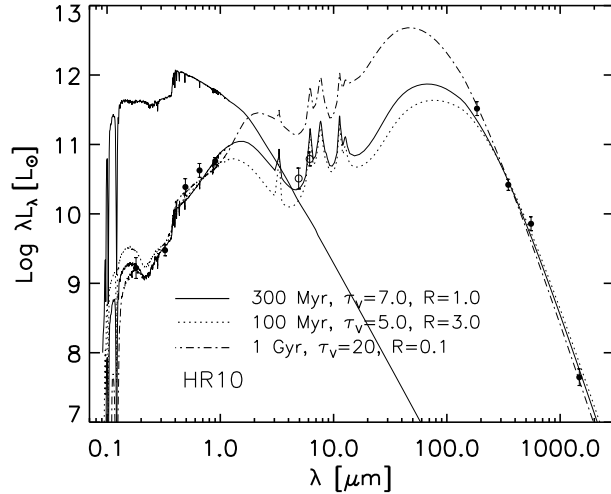


Fig. 20. The same as Figure 18d, but for the high redshift galaxy, HR10. ISO data are indicated by open circles. The MW extinction curve and $\eta = 1000$ are adopted for all models. The upper solid line in UV-NIR is the intrinsic stellar SED with $t = 300$ Myr.

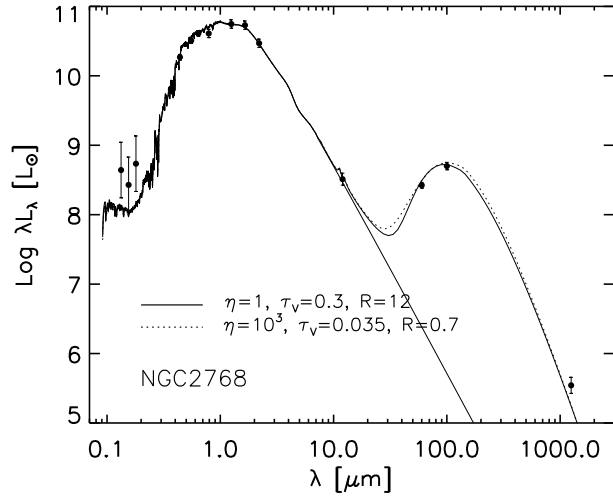


Fig. 21. The results of SED fitting for the elliptical galaxy, NGC2768. The MW type extinction curve and $t = 12$ Gyr are adopted for all models. The stellar emission (12 Gyr) in FIR is indicated by lower solid line.